University of California
Santa Barbara

Morphology-dependent optical anisotropies in organic semiconductors

A dissertation submitted in partial satisfaction
of the requirements for the degree

Doctor of Philosophy
in
Materials

by

Steven J. Brown

Committee in charge:

Professor Jon A. Schuller, Co-chair
Professor Christopher J. Palmstrøm, Co-chair
Professor Michael L. Chabinyc
Professor John E. Bowers

June 2017

The Dissertation of Steven J. Brown is approved.

Professor Michael L. Chabinyc

Professor John E. Bowers

Professor Jon A. Schuller, Co-chair

Professor Christopher J. Palmstrøm, Co-chair

May 2017

Morphology-dependent optical anisotropies in organic semiconductors

Steven J. Brown

For my parents.

Acknowledgements

There are many people who made this thesis possible. First, I would like to thank my research colleagues. Richard Grote did many of the initial calculations and simulations which demonstrated that molecular orientation is a crucial design parameter in light trapping solar cells – this provided the jumping off point for much of my thesis work. Ruth Schlitz helped me get started in organic electronics, provided the samples for our paper linking optical anisotropies to molecular structure, and shared her wisdom on how to be an effective researcher. Niva Ran provided the samples for our paper demonstrating how molecular orientation affects surface plasmon polariton properties in addition to many helpful discussions about research, organic chemistry and structure, and practical devices. Lance Park, Sam Willenson, and David Nakazono were undergraduate researchers who assisted in several of the experiments, lab automation, and data analysis. Kyle Arakaki was a masters student who did much of the initial work to automate the otherwise tedious momentum-resolved photoluminescence excitation measurements. Professors Guillermo Bazan, Thuc-Quyen Nguyen, and Michael Chabinyc provided research advice particularly with regard to molecule selection that I am sure saved me many hours of work. I am especially grateful to the amazing laboratory technicians we have at UCSB. In particular Brian Thibeault taught me how to use the spectroscopic ellipsometer, Jaya Nolt and Amanda Strom for their help with UV-Vis spectrocopy measurements, and Mark Cornish for his assistance with atomic force microscopy. I would also like to thank Jianing Sun, an application engineer at J.A. Woollam, for helping me analyze some of our ellipsometry data.

I would like to thank my lab group. Prasad Iyer has been a constant companion during my PhD and an endless source of interesting optics papers and discussion. Tanya Das has been a amazing listener on any topic and a great compatriot for many of my

extracurricular activities. Tomer Lewi, as someone who has done it all before, has provided much guiding wisdom as I have put together papers and worked through my PhD. I would also like to thank him for helping me remove the hanging tables in our lab so I did not suffer a permanent head injury. Nikita Butakov shared my interests in math and machine learning and has been a great balancing force in the group. Ryan DeCrescent has been my research partner for the past year and a half. I am especially happy to leave the optical setup that has been my baby for the past five years in his capable hands – with all the power and responsibility (a.k.a. alignment work) that it entails. Professor Jon Schuller has provided funding and guidance throughout my PhD. I am particularly grateful for the optical theory he taught me, the opportunity to grow into an independent researcher, his focus on good science and putting science first, and the random quantum mechanics and electromagnetism problems he would sometimes distract us with.

In addition to Jon, I would like to thank the rest of my thesis committee. Professor Christopher Palmstrøm co-advised me throughout my studies. He always gave a different perspective for looking at my research which helped me get out of several experimental ruts. Professor Michael Chabinyc has always been available when I needed guidance on organic materials or graduate school in general. Professor John Bowers provided a helpful critical eye to make sure the optical parts of our experiments were sound.

I would like to thank my friends, there are too many to list here, for keeping me sane throughout graduate school. In addition to great food and conversation, they shared their advice on the practice of science and dreams for what it could be.

Of course the list would not be complete without thanking my family. From a young age my parents encouraged me to pursue academic excellence. Over the years they have been truly steadfast in their support and I am forever grateful. My adventure partner Jamie Wilcox has been a wellspring of encouragement and fine baked goods. Perhaps she deserves the most thanks of all as she has stuck by me throughout the making of this

thesis.

Curriculum Vitæ

Steven J. Brown

Education

2017	Ph.D. in Materials (Expected), University of California, Santa Barbara.
2011	B.S. in Physics, University of Minnesota, Twin Cities.
2011	B.S. in Mathematics, University of Minnesota, Twin Cities.

Experience

June 2016-Sept. 2016 Data science intern, Citrine Informatics

Teaching

2013	Teaching assistant, Electronic Properties of Materials

Service

2015-2017	Founder and president, Data Science Learning Group
2014-2016	Founding member, co-president, and head of logistics, Beyond Academia
2014-2017	Member, website chair (2015-2016), and survey chair (2014-2015), Graduate Students for Diversity in Science

Mentoring

Trained and mentored a total of 6 undergraduate and masters-level researchers throughout my time at UCSB including David Nakazono, Samuel Willenson, Kyle Arakaki, Lance Park, Norah Hoffman, and Dashiell Bodington.

Awards

- Best oral contribution, Symposium: The Grand Challenges in Organic Electronics, MRS Spring 2014

Publications

- **Brown, S. J.**, DeCrescent, R. A., Nakazono, D. M., Willenson, S. H., Ran, N. A., Nguyen, T-Q, & Schuller, J. A., Orientation-dependent surface plasmon polaritons in out-of-plane uniaxial films. In preparation.
- **Brown, S. J.**, Schlitz, R. A., Chabinyc, M. L., & Schuller, J. A., Morphology dependent optical anisotropies in the n-type polymer P(NDI2OD-T2). *Phys. Rev. B* **94**, 165105 (2016).

- DeCrescent, R. A., **Brown, S. J.**, & Schuller, J. A., Model-blind characterization of thin-film optical constants with momentum-resolved reflectometry. *Opt. Express* **24**, 28842–28857 (2016).
- Grote, R. R., **Brown, S. J.**, Driscoll, J. B., Osgood, R. M. & Schuller, J. A. Morphology-dependent light trapping in thin-film organic solar cells. *Opt. Express* **21**, A847–A863 (2013).

Presentations

- Measurement of optical anisotropy in organic semiconductors, *South China University of Technology - University of California, Santa Barbara Joint Workshop*, Guangzhou, China (January 12, 2016).
- Measuring optical anisotropies in organic semiconductors, *SPIE Optics and Photonics*, San Diego, CA, USA (August 12, 2015).
- Morphology-dependent optical properties of polymer materials, *Chemical Sciences Student Seminar*, Santa Barbara, CA, USA (October 13, 2014).
- Morphology-dependent optical properties of polymer and small molecule materials, *SPIE Optics and Photonics*, San Diego, CA, USA (August 21, 2014).
- Morphology-dependent optical properties of small molecule and polymer materials, *Materials Research Society Spring Meeting*, San Francisco, CA, USA (April 24, 2014).

Abstract

Morphology-dependent optical anisotropies in organic semiconductors

by

Steven J. Brown

Organic semiconductors tend to have highly ordered, anisotropic morphologies. These structural anisotropies lead to optical anisotropies which we have shown directly affect the efficiency of photonic devices such as organic photovoltaics (OPVs). Measuring the direction-dependent optical properties of organic films would thus give unique insights into film structure and inform the design of organic optoelectronics. In this work we develop momentum-resolved spectroscopies to precisely measure the emitting and absorbing dipole strengths as well as complex refractive indices of uniaxial organic films. We then demonstrate how these techniques can be used to investigate film morphology by measuring the tilt angle and processing-dependent structural changes in the polymer system P(NDI2OD-T2). Finally, we show how molecular orientation impacts device properties by studying changes in surface plasmon dispersion and photoluminescence enhancement in films of the small molecule p-SIDT(FBTTh$_2$)$_2$ on gold.

Contents

Chapter 1

Introduction

Organic optoelectronics have seen sustained interest for over half a century. They are inexpensive to manufacture[1], made from abundant materials, eminently chemically tunable for a variety of applications[2], and potentially physically flexible[3]. The past fifteen years in particular have seen a resurgence of research into organic photovoltaics (OPVs). OPVs have held great promise for next generation renewable energy. Yet even after best-in-class lab cells have surpassed the 10% efficiency milestone[4] long claimed to be the bar for commercialization, OPVs have not seen widespread use outside of the laboratory. There is more work to be done for OPVs to reach their potential.

It has become clear that for continued improvement the relationship between material morphology and electronic properties must be understood[5, 6, 7]. Organic semiconductor molecules typically have a planar or rod-like structure. These anisotropic molecules then self-assemble into films which in turn have anisotropic electric and optical properties. To achieve the highest possible efficiency, these anisotropies must be taken into account when designing devices. Prior work has shown charge transport anisotropy to strongly affect final device performance.[8] My colleagues and I have calculated that optical anisotropy also has strong effects on final device performance.[9] Using analytical

calculations and finite-difference time-domain simulations, we compared two orientations of the benchmark polymer poly(3-hexylthiophene-2,5-diyl) (P3HT): the as-spun morphology with polymers lying in the plane of the substrate and a model orientation with polymers perpendicular to the substrate. We looked at both surface plasmon polariton (SPP) and gap-mode light trapping architectures. We found significant changes to both absorption and the effective complex refractive index depending on polymer orientation. In these ultra-thin light trapping architectures, reorientation of P3HT could *by itself* increase light absorption over the solar spectrum by greater than a factor of two.

Furthermore, while there have been many previous studies on charge transport anisotropies [10, 11, 6], there has been less work looking at optical anisotropies. In particular, measuring the dielectric tensor in the direction perpendicular to the film plane (the so-called out-of-plane direction) is challenging using traditional techniques. Most of these techniques probe the material with light incident from air. Because light bends towards the surface normal when entering a higher index medium, the probing light propagation direction ends up near-normal in the material of interest with an electric field pointing almost entirely in the plane of the sample (in-plane). For example, light incident at a grazing incidence of 80° from air will propagate at 41° upon entering a material with a refractive index $n = 1.5$. This results in low sensitivity to out-of-plane optical constants which are much more important than in-plane constants when designing solar cells with light trapping architectures.

In this work we develop momentum-resolved spectroscopy techniques to investigate optical anisotropies in organic films. These techniques are able to precisely measure absorption, photoluminescence, and reflection as a function of light momentum (angle). By using high numerical aperture (NA) optics, high momenta modes are accessed in the material of interest leading to greater sensitivity to out-of-plane optical constants. Collaborators and I have demonstrated in detail that compared to variable angle spec-

troscopic ellipsometry (VASE),[12] the current state of the art technique for measuring anisotropic optical constants, momentum-resolved spectroscopy is more sensitive to out-of-plane optical properties and enables free-parameter free, or "model blind", fitting of optical constants.[13] In particular, building ellipsometric models for anisotropic organic materials is especially challenging: model free parameters can often exceed 30 or more leading to a huge parameter space to fit over with possibly many local minima that do not accurately describe the material in question.

Chapter 2 will detail the concepts behind momentum-resolved spectroscopy, how our apparatus is constructed, how various measurements are performed, and how to analyze the resulting data to extract relevant material properties. In particular, we extend previous momentum-resolved spectroscopy techniques, which only resolved emitted light momenta, with the ability to precisely choose the input light momentum as well. This enables new spectroscopies for studying absorption and reflection anisotropies.

In Chapter 3 we then apply these momentum-resolved techniques to discover both how anisotropic optical properties can reveal subtle structural information (e.g. crystallinity) as well as how structural anisotropy leads to anisotropic optical properties such as the dipole tilt angle.

In Chapter 4 we experimentally demonstrate how optical anisotropy affects device properties. We show how molecular orientation affects optical coupling, by measuring changes in surface plasmon polariton mode dispersion and photoluminescence enhancement as a function of film morphology.

Chapter 5 discusses potential future avenues for research. Many of the areas are enabled by our apparatus which resolves both output and *input* light momenta. In particular the rich set of problems that can be tackled using structured light input will be discussed.

1.1 Permissions and Attributions

1. The content of Chapter 3 is the result of a collaboration with Ruth A. Schlitz, Michael L. Chabinyc, and Jon A. Schuller, and has previously appeared in Physical Review B.[14] It is reproduced here with the permission of the American Physical Society: `https://www.aps.org/`.

Chapter 2

Momentum-resolved imaging and spectroscopy

2.1 Introduction

Investigating anisotropic optical properties requires the ability to study how light interacts with a sample as a function of angle, i.e., measuring the incident, reflected, or emitted light intensity versus angle. There are three main ways to do this: tilt the sample, move the detector, or place a 2D detector in the Fourier plane of the sample. It is challenging to get high angular resolution when simply tilting the sample and it's more complicated to extend the measurement, such as adding a prism to access grazing angles of light in the material. Moving the source and detector on arms (i.e. a goniometer) allows for a more precise measurement of the angle and it's easier to modify the experiment. Fourier space measurements go a step further. By placing a 2D detector in the Fourier plane, this technique measures all angles *simultaneously* at high resolution and, by using a high numerical aperture (NA) objective, can measure light at angles greater than the critical angle in the sample. Spectroscopies based on this technique are called momentum-

resolved as they resolve the momentum (angle) of the input or output light. As mentioned in Chapter 1, momentum-resolved spectroscopies have a number of advantages over state-of-the-art variable angle spectroscopic ellipsometry (VASE) which is typically used for studying anisotropies in organic semiconductors.

Fourier space spectroscopy works by placing the source or detector in the back focal plane (BFP) of an imaging objective. Points in the BFP correspond to specific momenta of light incident or emitted from a sample as opposed to specific positions of light usually detected in a traditional imaging setup. By correctly placing an additional lens in an imaging setup, the BFP can be re-imaged at a detector or source. We call this re-imaged plane a conjugate BFP of the objective. This technique is extremely versatile and by adding a polarizer, spectrometer, or pulsed source it can be extended with polarization, energy, or time resolution. Indeed, Fourier space imaging is the momentum space equivalent of real space imaging and supports the same multitude of spectroscopies.

These momentum-resolved methods have been used to study a broad range of phenomena including the orientation of single molecules[15], multipole emission in nanoparticles[16], magnetic dipole emission in phosphors[17], intra- and intermolecular excitons[18], radiation leakage in surface plasmon polariton waveguides[19], and radiation patterns of nanoantennas[20] among others. By extending previous techniques with momentum-resolution for the incident light source, we can now study absorption and reflection as well as emission in all of these systems. We can probe how properties in these systems change when specific angles or modes are pumped. This enables, for example, exciting an isolated exciton type and watching how it decays into potentially multiple exciton species. Many of these potential applications are discussed in Chapter 5, Outlook and future work.

Momentum-resolved photoluminescence (mPL), momentum-resolved photoluminescence excitation (mPLE), and momentum-resolved reflectometry (mR) are of particular

interest for studying organic semiconductors. mPL measures the output PL as a function of angle and can be decomposed into PL spectra for emitting dipoles in the plane of the sample (in-plane) and perpendicular to the sample plane (out-of-plane). mPLE measures total PL as a function of incident light angle and energy. The amount of PL is used as a proxy for the amount of light absorbed, and mPLE can be thought of as the absorption equivalent of mPL. mR measures the amount of light reflected as a function of incident angle and energy. In-plane and out-of-plane complex dielectric functions can be extracted by fitting mR data.

In this chapter we will discuss how to implement these spectroscopies. First we'll discuss the apparatus we constructed and how it can be configured for different types of experiments. Along the way I will point out key features and design considerations for performing high-resolution measurements. Then we will step through how to analyze the resulting data to extract intrinsic material properties.

2.2 Instrumentation

To perform a wide range of momentum-resolved spectroscopies, including first-ever mPLE and mR measurements, we built an apparatus particularly well-suited for these techniques. This section discusses the various components of the instrument, configurations for different measurement techniques, and practical considerations for achieving high resolution measurements.

Figure 2.1 shows a diagram of the constructed setup while Figure 2.2 displays a corresponding photograph. Figures 2.3 and 2.4 give a more detailed view of the input and output optics including spacings. Crucially, lenses are arranged such that both the light source and analyzing spectrometer are in BFPs conjugate to the sample objective BFP. This allows for momentum resolution on both the input and output. Additionally

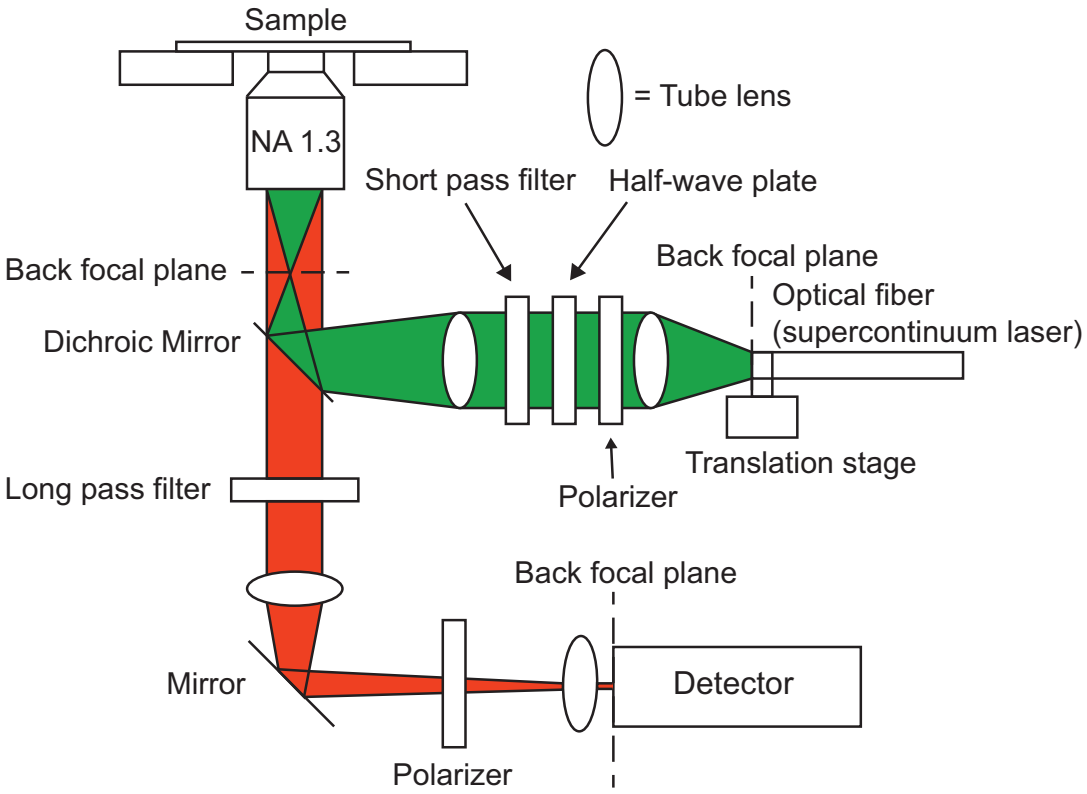

Figure 2.1: The constructed momentum-resolved setup. For momentum-resolved photoluminescence, the supercontinuum excitation source along with the half-wave plate, polarizer, and first tube lens were replaced with a collimated LED. For momentum-resolved reflection the filters are removed and the dichroic mirror is replaced with a 50/50 mirror. (Reproduced from Brown[14])

we resolve the energy on the input by using a supercontinuum source (SuperK Extreme EXR-15) with monochromator (NKT Photonics SuperK Select IR2 Vis/NIR) and on the output by using a spectrometer (Princeton Instruments IsoPlane SCT320) and attached charge coupled device (CCD) camera (Princeton Instruments PIXIS 1024BRX). This allows us to simultaneously measure energy and momentum and enables so-called energy-momentum spectroscopies such as mPLE and mPL. The polarization optics on the input and output discriminate between p-polarized and s-polarized light which leads to greater differentiation between optical dipoles in the sample plane versus perpendicular to the plane. By using a 1.3 numerical aperture (NA) objective the region of high momenta

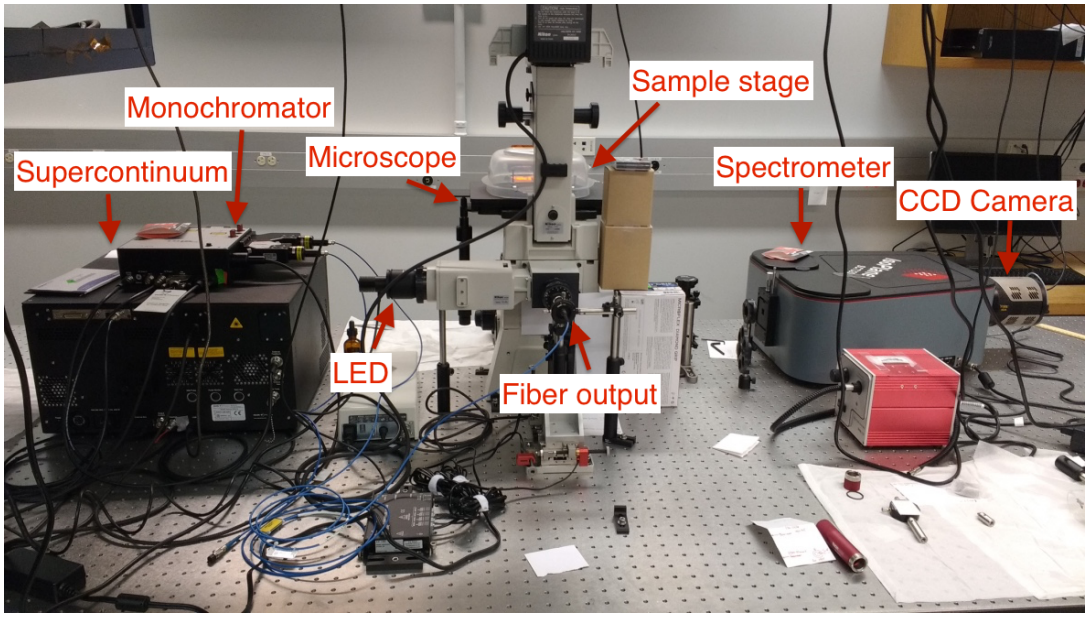

Figure 2.2: Picture of the constructed momentum-resolved setup. A mirror is slid into place to switch from the fiber-coupled supercontinuum source to an LED source.

past the critical angle, where much of the information to distinguish dipole orientation exists, can be measured.

There are multiple possible configurations of the apparatus depending on the measurement being performed. Figure 2.1 shows a generic configuration with momentum resolution of both the input and output light.

To configure the setup for mPLE, the analyzing polarizer is removed and all PL is collected. The diffraction grating in the spectrometer is set to the zero-order mode such that there is no separation of light based on wavelength and the sum of counts on the CCD is recorded, essentially turning the detector into a simple photodiode. In this arrangement the fiber-coupled light source is a point source in a BFP conjugate to the objective BFP. By moving the fiber in this plane via a translation stage (driven by Newport Picomotor actuators), the incident momentum, parallel to the sample, of the light is varied. Light at normal incidence ($k_{\parallel} = 0$) excites only in-plane optical dipoles, while p-polarized light at the critical angle ($k_{\parallel} = k_0$) excites only out-of-plane dipoles.

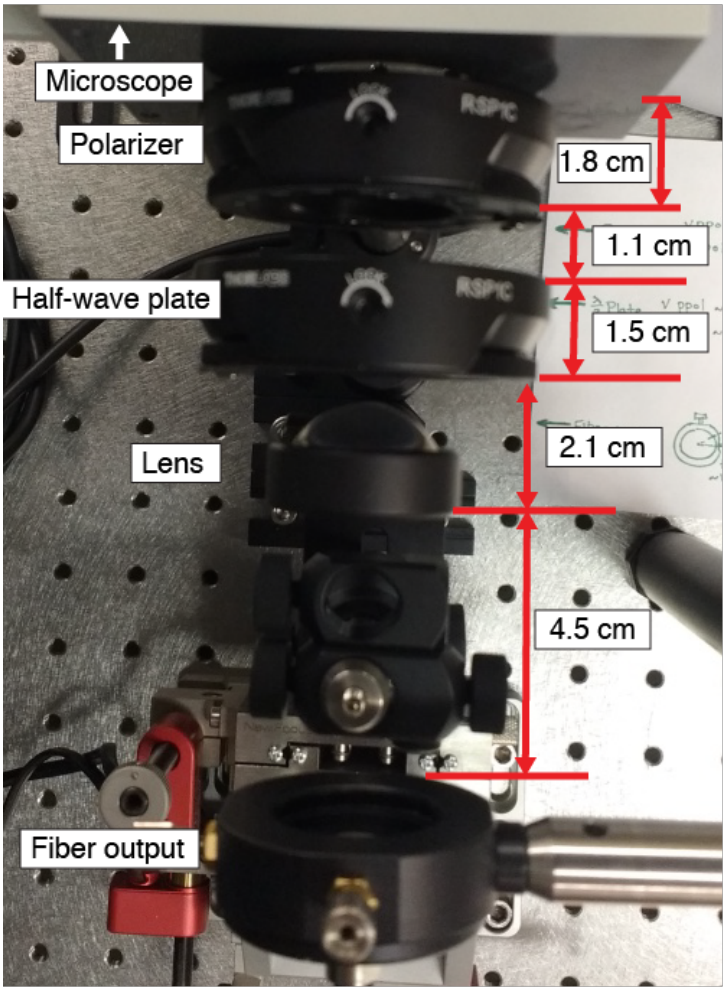

Figure 2.3: Picture of input optics with distances labeled.

To configure the setup for mPL, the fiber, polarizer, half-wave plate, and first tube lens are replaced with a collimated LED. This uniformly illuminates momentum space. The emitted light is then analyzed with a polarizer and spectrometer. With this measurement it is possible to get independent PL spectra and effective emitting dipole strengths for in-plane and out-of-plane oriented dipoles.

To configure the setup for mR, the filters and analyzing polarizer are removed and the dichroic mirror is replaced with a 50/50 mirror. Additionally, due to the high laser brightness it is sometimes necessary to add optical density filters to the input. By scan-

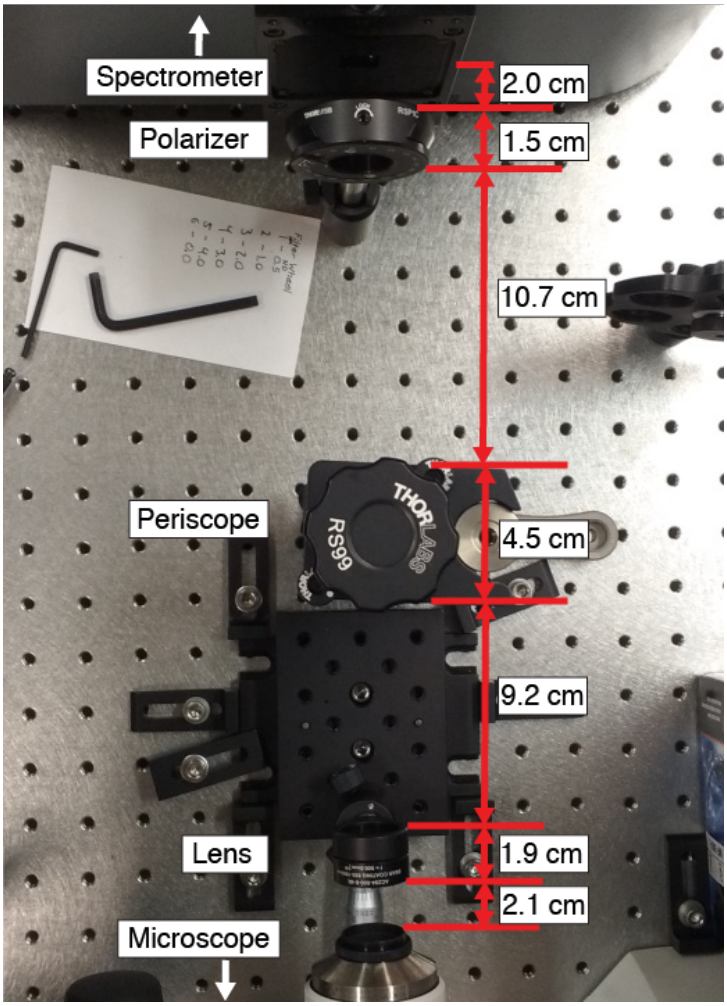

Figure 2.4: Picture of output optics with distances labeled. The periscope is only necessary to shift the beam higher with respect to the table since the exit of the microscope and entrance of the spectrometer are at different heights.

ning the output fiber in momentum space, it is possible to construct a complete reflection versus momentum curve. Alternatively, by placing a stack of diffuser films in front of the laser fiber, it is possible to uniformly illuminate momentum space, thereby allowing for measurement of the entire reflection versus momentum curve in a single measurement. Typically, one also varies the input wavelength to measure how the reflection versus momentum curves change with wavelength.

There are several considerations for achieving high resolution, low aberration

momentum-resolved measurements, some of which are the same as real space measurements and several that are unique to momentum space. Importantly, momentum space is the Fourier transform of real space. Light that has a well-defined position in real space is extremely spread out in momentum space and vice versa. This has the immediate consequences when trying to adapt a microscope setup built for traditional real space imaging. Light that is focused in momentum space will be collimated and spread out over a large area as it travels between the conjugate BFP of the source and the BFP of the objective. Narrow tubes and apertures used to cut down on noise in real space measurements can clip the collimated light beam in momentum space measurements. Where possible, these apertures and narrow tubes should be removed. Ideally, optics that are large compared to the collimated beam footprint should be used to avoid clipping and maintain a wide range of accessible momenta.

Microscope objectives are generally not optimized for momentum space measurements and there are several momentum-space-specific aberrations possible (see Kurvitz[21] for an in-depth discussion of these aberrations). The most prominent of these is momentum space vignetting where high momenta light is reduced in intensity. This vignetting should be measured with a well-know reference (such as quartz reflection) and corrected for in data analysis either only using data below a certain momenta or by adjusting the intensity to account for the reduction due to the objective. For the lowest aberration, high NA Plan Apo objectives should be used while total internal reflection fluorescence (TIRF) objectives should be avoided.[21]

Similar to real space measurements, momentum-resolved measurements should be well focused. See Appendix B for detailed instructions on correctly focusing and aligning the apparatus. Having optics out of focus makes separating light from in-plane and out-of-plane dipoles challenging as they are mixed at the "critical angle" in an out of focus BFP. In particular, achromatic optics should be used to maintain a sharp BFP

across wavelengths. Additionally, polarization preserving and insensitive optics should be used throughout to ensure s-polarized and p-polarized light have the same BFP and to preserve the polarization which helps discriminate in-plane versus out-of-plane dipoles in mPL and mPLE.

In the case of using a CCD camera to record the output light, one must be aware of electronic noise. There is typically a base noise level whenever data is read out of the camera. To keep the signal-to-noise ratio high, data should be read out as infrequently as possible (i.e. long exposure times with a single exposure instead of short exposure times with multiple exposures). Additionally, the background noise due to both stray light and electronics should be subtracted during data analysis.

2.3 Analysis

Extracting relevant material parameters from observed data requires a careful analysis taking into account how the data is produced. The theory for this modeling has already been well-developed by Schuller[18] and Taminiau[17] and readers are referred to the supplementary information of those papers for a complete treatment of the theory. With an optical model of data generation in hand, it is possible to deterministically fit momentum-resolved spectroscopy data to derive intrinsic material properties such as anisotropic complex refractive indices, emission and absorption dipole strengths, and molecular orientation.

Here we will focus on practically implementing the optical model and using it for a complete analysis of the in-plane and out-of-plane effective dipole strengths from mPL and mPLE. For extracting anisotropic complex refractive indices using mR, please refer to DeCrescent.[13]

Momentum-resolved photoluminescence analyzes the energy and momentum of emit-

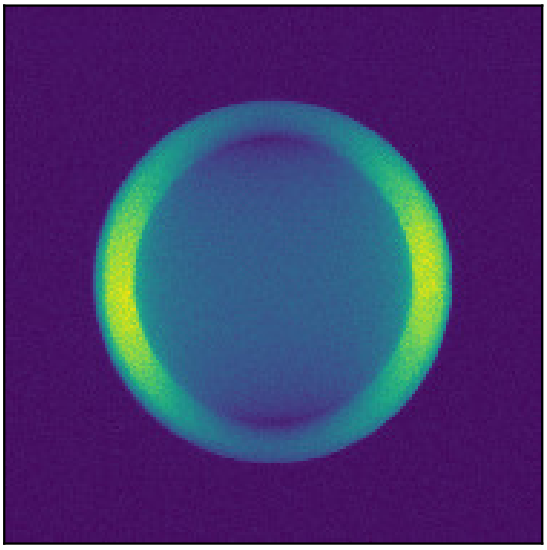

Figure 2.5: A raw back focal plane image of photoluminescence passing through a y-oriented polarizer.

ted light. By setting the detector in a conjugate BFP to the objective, a momentum-space image of the PL (Figure 2.5) can be taken. An analyzing polarizer is set in path to additionally discriminate light emitted by in-plane and out-of-plane dipoles. By passing a thin vertical sliver of light in the BFP through a slit into a spectrometer, light can be separated into wavelength along the x-axis and $k_{\|}$ momentum along the y-axis (Figure 2.6).

While the wavelength for each column in Figure 2.6 is known from prior calibration of the spectrometer, the momentum still needs to be labeled. The PL extends to NA limit of the objective (i.e. a 1.3 NA objective will capture PL to $\pm k_{\|}/k_0 = 1.3$); this fact can be used to label pixels with their associated momenta. There are many ways to find the edges of PL for the momentum labeling. Appendix A.1 contains the code to implement a simple sliding window algorithm for this purpose. The red dots in Figure 2.7 are example PL edges for a single wavelength column determined using this algorithm.

Once the pixels are labeled, one can decompose the counts into those coming from

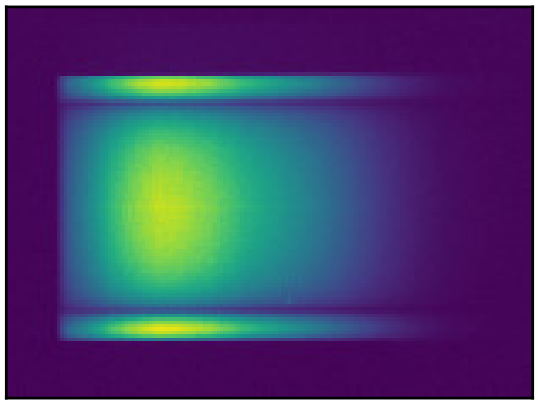

Figure 2.6: A raw energy-momentum spectrum image. Light is separated by $k_{\|}$ along the y-axis and wavelength along the x-axis.

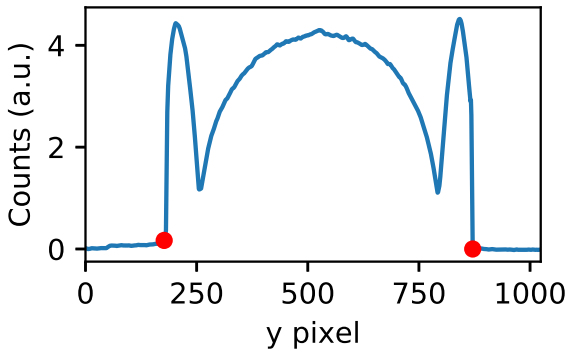

Figure 2.7: Pixel intensities for a column from an energy-momentum spectrum image. The red circles denote the edge of photoluminescence which have momentum $\pm k_{\|}/k_0 = NA$

in-plane and out-of-plane dipoles with a three layer model (see Appendix A.2 for an implementation of the model). The shape of the counts versus momentum curves are different for in-plane and out-of-plane dipoles. This leads to a unique linear combination of in-plane and out-of-plane counts that best fit the data (see Figure 2.8). This decomposition is implemented in the `fit_dip_strengths` method in Appendix A.3. Note that in the case of mPL measurements the three-layer model includes a $\frac{1}{\cos\theta} = \frac{n*k_0}{k_z}$ correction for apodization (for θ, n, k_z in the collection layer, typically a quartz substrate).

Here apodization refers to intensity variations due to each pixel in the BFP capturing a different solid angle of PL. High momentum pixels capture a larger swath of solid angle resulting in isotropic emitters having non-isotropic BFP intensity images which needs to be accounted for.

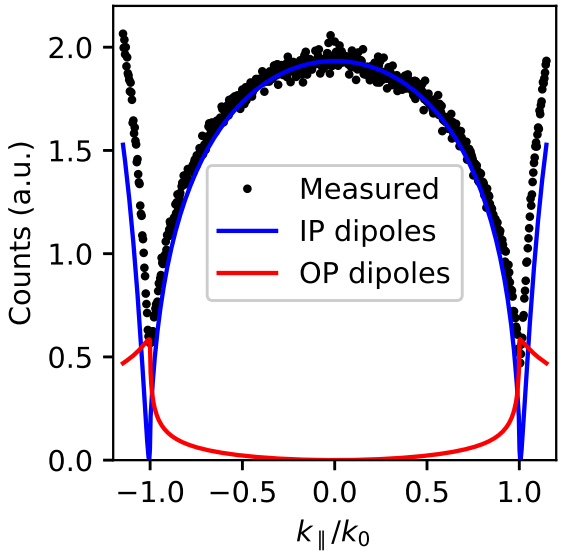

Figure 2.8: Decomposition of photoluminescence counts into counts coming from in–plane (IP) and out-of-plane (OP) dipoles.

From this decomposition one can divide out the density of optical states and extract the effective emission dipole strengths for in-plane and out-of-plane dipoles. The effective dipole strength is the product of the number of emitting dipoles and the oscillator strength of each dipole in a given direction. Plotting the effective dipole strengths at each wavelength (Figure 2.9) gives an "intrinsic" spectrum of the material. This is a rich source of information containing details such as the spectra of different excitations[18], the orientation of the transition dipole[14], and the relative number of in-plane and out-of-plane dipoles (Chapter 4).

Momentum-resolved photoluminescence excitation is the absorption equivalent of mPL. In mPLE the total PL is measured as the momentum and wavelength of the

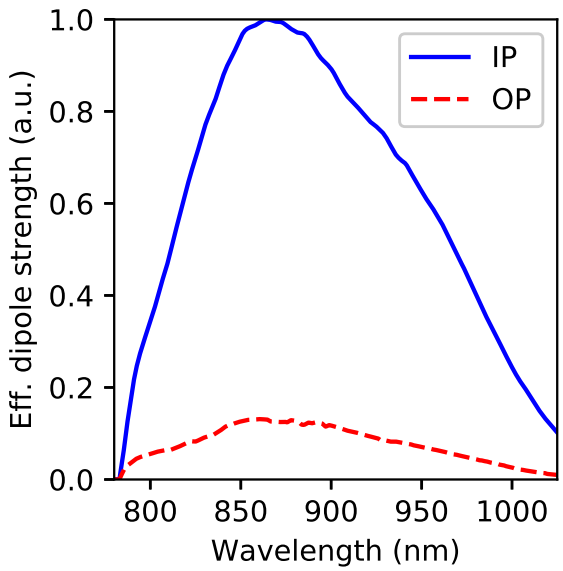

Figure 2.9: In-plane (IP) and out-of-plane (OP) effective dipole strengths.

incident light is varied. See Figure 2.10 for a BFP image of a typical laser spot used in mPLE. Analyzing mPLE data is similar to mPL but for each combination of momentum and wavelength a single PL image is recorded and the total PL is calculated by summing counts over all pixels. By combining many of these images an intensity versus momentum curve is created. To then find dipole strengths versus wavelength, an intensity versus momentum curve must be built for each wavelength. It is important to note that mPLE does not have an apodization correction since the input power is fixed (it will just be more spread out in solid angle at higher momenta) and the total PL is collected. In general mPLE is more challenging than mPL: not only must many more images be collected, but the optical constants used in the three layer model vary greatly across the absorption region making the modeling more challenging.

It is important to properly subtract the background when performing mPLE. Due to subtle but significant background drift over time, the mean background counts should be calculated *for each PL image*. One effective method for calculating this background

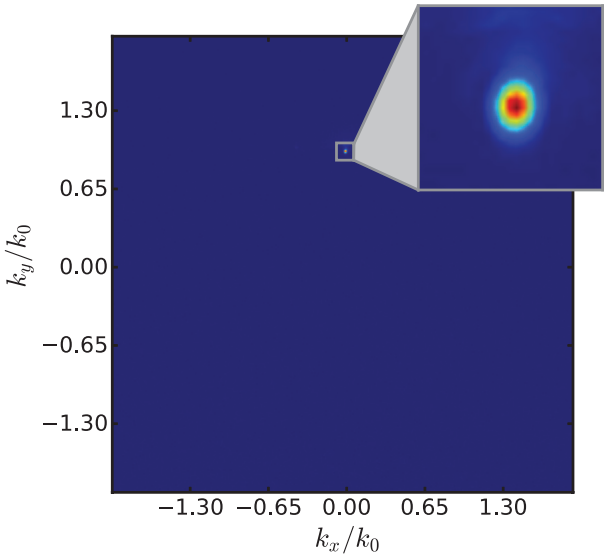

Figure 2.10: Back focal plane image of typical incident laser spot used for momentum-resolved photoluminescence excitation. Modified from Brown.[14]

is to find the mean counts per pixel in a "window frame" of the image outside the PL region (see Figure 2.11). This mean background count is then subtracted from each pixel before summing over all pixels to get the total PL counts for the image.

2.4 Conclusion

In this chapter we introduced momentum-resolved spectroscopies. These spectroscopies place either a source or detector in the back focal, or Fourier, plane of an imaging objective and are advantageous compared to conventional variable angle spectroscopic ellipsometry in studying optical anisotropies in organic semiconductors. While discussing the construction of our apparatus in detail, we highlighted salient points in the design of momentum-resolved instruments including the inherent trade-off between spot size in real space and momentum space. Our apparatus resolves input as well as output momentum which immediately enables new spectroscopies and areas of investigation particularly in the pumping of specific excitations. The measurements of momentum-resolved photolu-

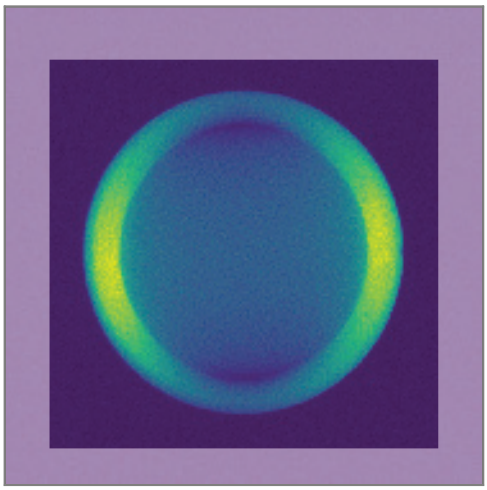

Figure 2.11: To calculate mean background counts per pixel in a back focal plane image, a window frame, denoted here by the lighter outside border, outside the PL region is used.

minescence, momentum-resolved photoluminescence excitation, and momentum-resolved reflectometry and their analysis was discussed. These are used to measure emission dipole orientation and strength, absorption dipole orientation and strength, and anisotropic optical constants, respectively.

Chapter 3

Morphology-dependent optical anisotropies

3.1 Abstract

Organic semiconductors tend to self-assemble into highly ordered and oriented morphologies with anisotropic optical properties. Studying these optical anisotropies provides insight into processing-dependent structural properties and informs the photonic design of organic photovoltaic and light-emitting devices. Here, we measure the anisotropic optical properties of spin-cast films of the n-type polymer P(NDI2OD-T2) using momentum-resolved absorption and emission spectroscopies. We quantify differences in the optical anisotropies of films deposited with distinct face-on and edge-on morphologies. In particular, we infer a substantially larger out-of-plane tilt angle of the optical transition dipole moment in high temperature annealed, edge-on films. Measurements of spectral differences between in-plane and out-of-plane dipoles, further indicate regions of disordered polymers in low temperature annealed face-on films that are otherwise obscured in traditional X-ray and optical characterization techniques. The methods and analysis

developed in this work provide a way to identify and quantify subtle optical and structural anisotropies in organic semiconductors that are important for understanding and designing highly efficient thin film devices.

3.2 Introduction

Organic semiconductors hold great promise in optoelectronic applications such as organic photovoltaics (OPVs)[22] and organic light emitting diodes (OLEDs)[23] due to their ease of processing (potentially leading to high-throughput and low-cost manufacture) and molecular tunability. Organic semiconductors typically self-assemble into highly ordered and oriented morphologies. As such, great strides have been made in characterizing and optimizing morphologies[24, 25, 26, 27, 28], with a particular focus on the electrical[29, 30] and optical[31, 32, 33] properties relevant to devices. As most morphologies are highly oriented, it is important to study the variation of these properties along different directions. For instance, anisotropic electrical properties of organic semiconductors directly impact charge transport[10, 11, 6] and must be accounted for in device design[8]. Optical spectroscopies such as ellipsometry[34, 12], polarized absorption[35], polarized photoluminescence[36], and Raman[37, 38], similarly reveal anisotropic optical properties related to the refractive index, absorption, emission, and vibrational modes that significantly impact the design and efficiency of light-emitting[39, 40] and photovoltaic[41, 9] devices.

Recently, momentum-resolved photoluminescence (mPL) measurements have provided new insight into magnetic dipoles in atomic systems[17], intra- and inter-molecular excitons in H-aggregates [18], and waveguide exciton polariton modes [42]. Here, we extend these techniques to study absorption as well as emission properties in highly ordered polymer films. We study the molecule P(NDI2OD-T2) which adopts distinct

'edge-on' or 'face-on' orientations depending on processing conditions. By characterizing the optical anisotropies of both morphologies, we determine the average orientation of the transition dipoles, and resolve subtle differences in morphology (in both crystalline and non-crystalline regions). These results reveal structural features previously invisible to diffraction techniques and suggest ways to increase device performance through film morphology optimization.

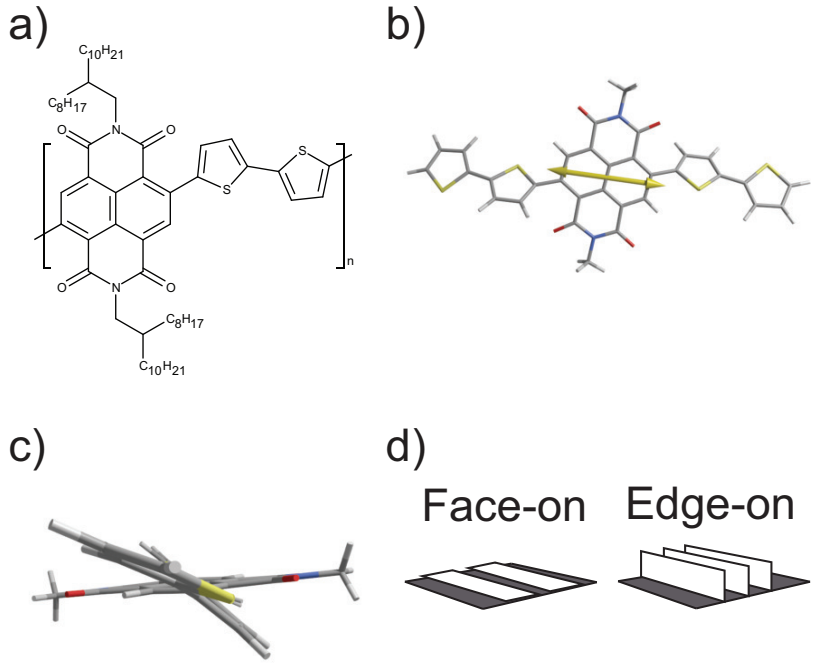

Figure 3.1: a)The chemical structure of P(NDI2OD-T2). b) Geometry and transition dipole moment of a P(NDI2OD-T2) molecule, determined with DFT calculations. The transition dipole moment (yellow arrow) lies in the plane of the NDI unit and is angled slightly with respect to the backbone. The alkyl side-chains have been truncated for visibility. c) A view down the backbone showing the relative twist of thiophene units with respect to the NDI2OD unit. While the subunits are twisted for both isolated and crystalline polymer, the exact angle in the solid state is dependent on morphology. d) When annealed at 150°C or 305°C P(NDI2OD-T2) takes on a face-on or edge-on morphology, respectively. The planes shown refer to the orientation of the NDI2OD planes.

P(NDI2OD-T2), sold by Polyera as N2200, is an n-type polymer. See Fig. 3.1(a) for its structural formula and Fig. 3.1(b,c) for geometry. As n-type semiconducting polymers

are rare, P(NDI2OD-T2) has been the subject of extensive morphology[43, 44, 45, 46, 47, 48, 49] and charge transport[50, 51, 52, 53, 54] studies.

P(NDI2OD-T2) is a particularly interesting system for studies of structure-function relations because its molecular orientation can be controlled through processing. Annealing films at a low temperature (150°C) results in a face-on morphology where the pi-stacking direction is perpendicular to the substrate (see GIWAXS, Appendix C.2, Fig. C.S1). In contrast, a high temperature anneal (305°C) results in an edge-on morphology with both the pi-stacking direction and polymer backbone parallel to the substrate.[55, 56] These two alternate morphologies are illustrated schematically in Fig. 3.1(d). Elucidating the effects various morphologies have on film function and device performance is on-going.

There have been a number of experiments linking processing conditions to optical properties. The excitations that lead to absorption and emission are thought to arise primarily from the $S_0 \rightarrow S_1$ ground state to first excited state transition on individual polymer chains.[46] Previous optical studies of P(NDI2OD-T2) in various solvents as well as in thin films reveal subtle differences in absorption and photoluminescence (PL) spectra depending on the degree of aggregation.[57, 58, 59] However, the dipole orientation seems largely insensitive to long-range or pi-pi interactions[57] and is expected to largely match the transition dipole moment of a single molecule. In this case the TDM is tilted 8 degrees within the NDI plane (Fig. 3.1b) and we thus expect a purely in-plane TDM for face-on films and a TDM partially angled out-of-plane (8 deg) for edge-on films. Using rubbing, directional epitaxial crystallization, or epitaxy on oriented substrates researchers have defined a preferential in-plane alignment of the polymer chains.[35, 48] Polarized absorbance measurements then reveal in-plane optical anisotropies: the films primarily absorb light with electric fields primarily polarized along the chain axis.[35, 48] These studies demonstrate significant optical structure-function relationships. However, these

measurements of optical anisotropies require specialized processing techniques to achieve in-plane alignment and are insensitive to out-of-plane oriented optical properties. In this paper we use momentum-resolved spectroscopies to measure the anisotropic optical properties parallel vs. perpendicular to the substrate in films of P(NDI2OD-T2) deposited with standard processing conditions and exhibiting no preferred in-plane alignment over optical length scales.

3.3 Results and Discussion

3.3.1 Momentum-resolved spectroscopy

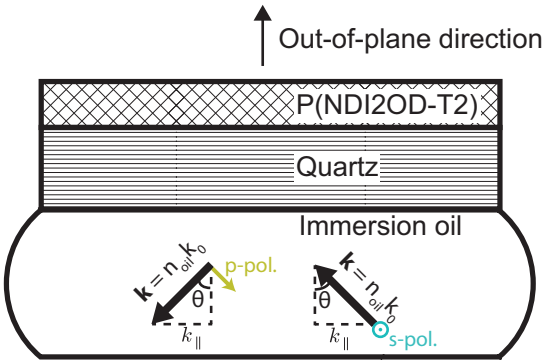

Figure 3.2: Schematic showing the measurement geometry. In mPLE, light is incident on the sample with a specific value of the in-plane momentum, $k_{||}$. In mPL light is emitted from the sample and measured as a function of $k_{||}$. The in-plane momentum is related to the angle of propagation as, $k_{||} = n_{oil} k_0 \sin\theta$. Both p-polarized and s-polarized light are independently measured for both techniques.

Momentum-resolved spectroscopies are a suite of techniques particularly well-suited to measuring the orientation of emitters, absorbers, and scatterers. In these techniques, variations in, e.g., PL, absorption, reflection, or scattered light intensity are measured as a function of the photon's momentum vector ($\vec{\boldsymbol{k}}$). These techniques utilize imaging in the back focal plane (Fourier plane) of a microscope objective (see Appendix C.1.1). Every point in the back focal plane corresponds to an angle of light incident on or emitted

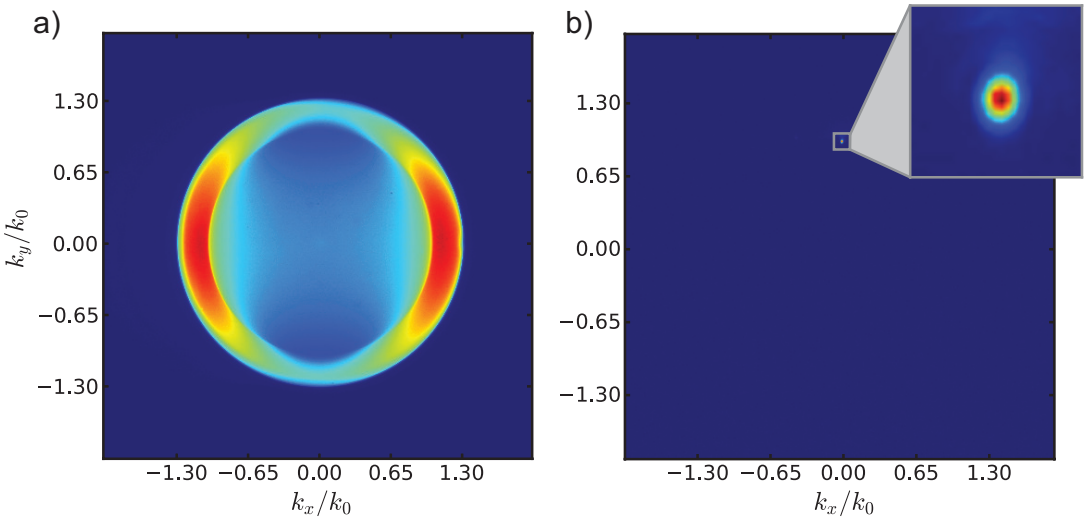

Figure 3.3: (a) False color back focal plane image of y-polarized photoluminescence (750-1050nm integrated) from a P(NDI2OD-T2) film. Vertical (horizontal) linecuts through the center correspond to p-polarized (s-polarized) traces. (b) False color back focal plane image of reflected laser light, demonstrating momentum-resolved excitation at $k_x = -0.02k_0$, $k_y = 0.96k_0$. By moving the output laser fiber within this plane we control the incidence momentum vector of our excitation source. The inset is a magnified image of the laser spot.

from the sample ($\theta = \arcsin\frac{k_\parallel}{nk_0}$, $\phi = \arctan\frac{k_y}{k_x}$ where $k_\parallel = \sqrt{{k_x}^2 + {k_y}^2}$); see Fig. 3.2 for the measurement geometry. For example, in Fig. 3.3(a) we plot the p-polarized mPL from a thin film of P(NDI2OD-T2). Following previously established procedures, [18] we decompose mPL measurements like these into contributions from in-plane and out-of-plane oriented emission dipoles. Similarly, we also extend this basic technique to measure the orientation of *absorption* dipoles. Incident light is focused to a point in the back focal plane, Fig. 3.3(b), such that it impinges the sample at a specific angle. By moving this focused light source within the back focal plane, we have complete control of the incident photon momentum vector and can measure momentum-resolved absorption. Both PL and absorption measurements are analyzed with simple electromagnetic models, detailed below.

Because the emission (and absorption) distribution of a dipole is anisotropic ($\propto$

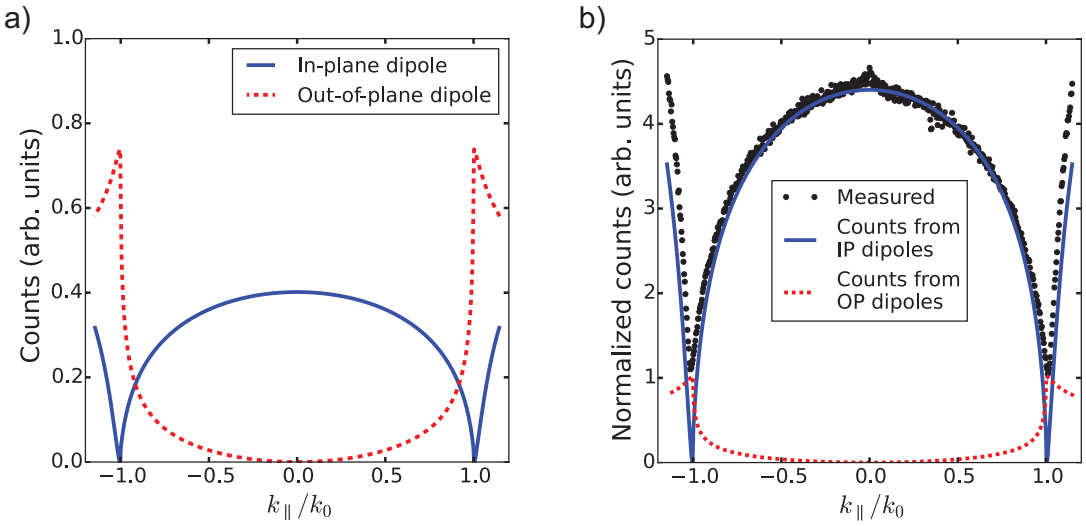

Figure 3.4: (a) Calculated momentum-dependent p-polarized luminescence expected from equal magnitude in-plane (blue, solid) and out-of-plane (red, dashed) emitting dipoles. (b) P-polarized photoluminescence at 865nm of P(NDI2OD-T2) annealed at 150°C decomposed into counts due to in-plane and out-of-plane dipoles.

$\sin^2\theta$), dipoles that are oriented in the plane of the sample (in-plane for the rest of the article) emit light into (or absorb light from) different angles than dipoles oriented perpendicular to the sample plane (out-of-plane). These differences are further amplified by reflections and interference in multi-layered geometries. Using a three-layer optical model, we calculate the p-polarized momentum-dependent PL intensity from purely in-plane (blue, solid) or out-of-plane (red, dashed) dipoles in a P(NDI2OD-T2) film, Fig. 3.4(a). The distributions are particularly different at normal incidence, where only in-plane (IP) dipoles emit, and at the critical angle, where only out-of-plane dipoles (OP) emit. We use these calculations to decompose measured momentum-resolved PL into contributions from IP and OP dipoles, Fig. 3.4(b). The 2D back focal plane PL image is focused to the entrance slit of an imaging spectrograph where it is separated spectrally. At each wavelength we measure the PL intensity as a function of in-plane momentum (black circles). The measured counts are decomposed into contributions from IP (blue, solid) and OP (red, dashed) dipoles. In this case, 5 percent of the total PL counts

originate from OP dipoles.

3.3.2 Emission and absorption anisotropy

Measured (solid, dot-dashed) and calculated (dashed) p-polarized (yellow, solid) and s-polarized (cyan, dot-dash) 865 nm PL traces for face-on and edge-on films are shown in Figs. 3.5(a,b). The s-polarized calculations contain no free fit parameters and show excellent agreement with measured PL up to approximately $k_{\|} = \pm 1.15 * k_0$. This value of $|k_{\|}|$ defines the range over which we perform fits of p-pol data—at larger momentum values the collection efficiency of the microscope objective begins to drop. The p-polarized experimental traces are fit according to the calculations described above, providing a measure of the relative contribution of in-plane and out-of-plane dipoles. As expected for excitations oriented primarily along the polymer chain, the emission in both morphologies is dominated by an in-plane dipole moment. However, fits of the p-polarized PL traces reveal a significant difference between the two morphologies. The ratio of out-of-plane to in-plane dipole moments is more than twice as large for edge-on (0.29) than face-on (0.13) morphologies. mPL allows us to resolve differences in the optical anisotropies that are *not* evident in ellipsometry (Appendix C.2, Fig. C.S2).

From mPL we derive the orientation of the transition dipole moment (TDM) with respect to the substrate. The ratio of OP to IP dipole moments translate into differences of the average inclination angle of the TDM with respect to the substrate. The inferred angle is $\arctan(0.13) = 7^\circ$ for face-on films compared to $\arctan(0.29) = 16^\circ$ for edge-on orientations. This increase in angle is consistent with the orientation of NDI planes in face-on versus edge-on films. DFT calculations indicate a TDM is oriented mostly, but not completely, parallel to the polymer backbone. The TDM is tilted (8°) in the NDI plane, see Fig. 3.1(b).[46, 51, 50] In the edge-on morphology, the TDM is thus partially

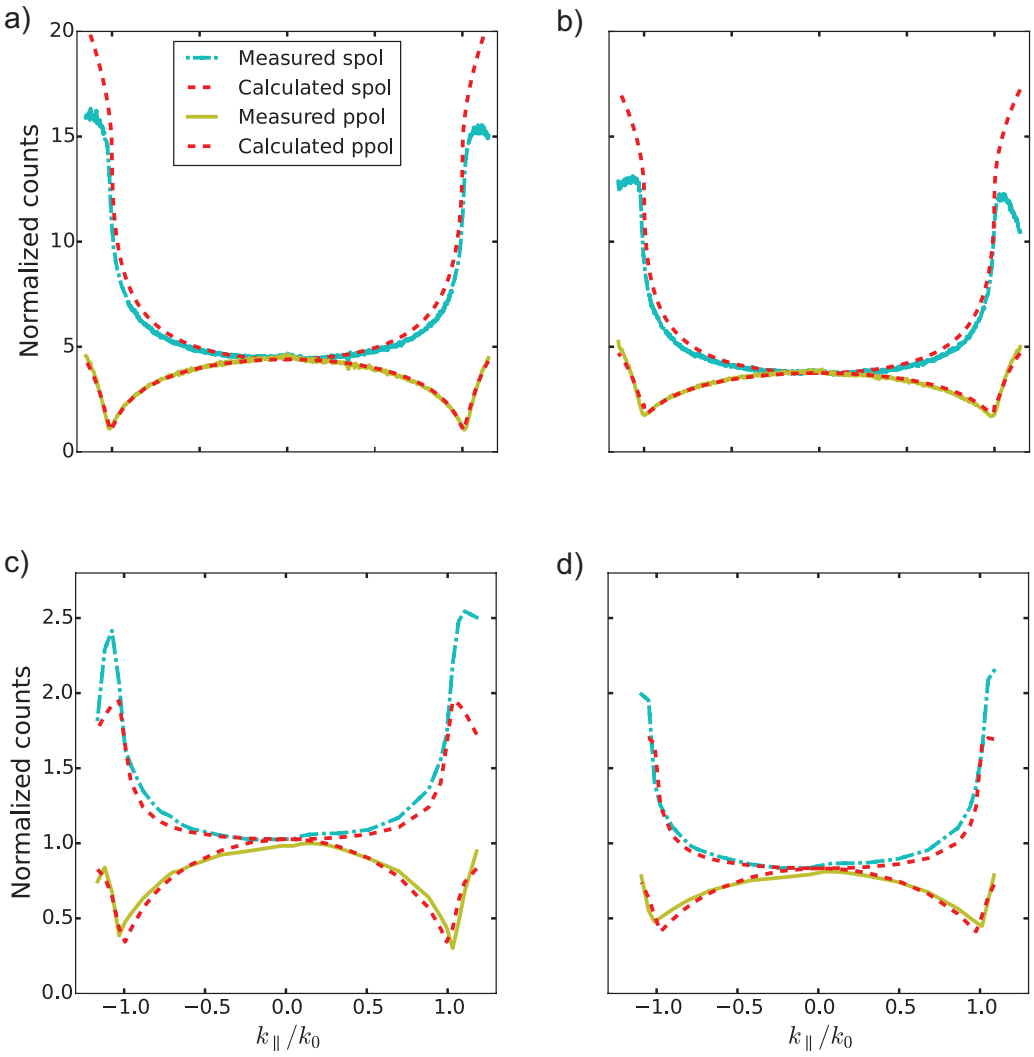

Figure 3.5: Examples of mPL measurements: 865nm photoluminescence intensity is recorded (solid, dot-dashed lines) vs. emission momentum for (a) face-on and (b) edge-on P(NDI2OD-T2). P-polarized traces (yellow, solid) are fit (dashed lines) to determine the relative contribution of IP and OP dipoles as illustrated in figure 4. From these fits we determine a predicted shape of the s-pol data (cyan, dot-dashed) with no free fit-parameters. The ratio of OP to IP dipole moments is 0.13 and 0.29 for face-on and edge-on films respectively. Examples of mPLE measurements: total photoluminescence intensity is recorded vs. incident momentum of 700nm excitation laser for (c) face-on and (d) edge-on P(NDI2OD-T2). The curves exhibit visible differences from mPL due to different values of the experimental apodization factor and values of the refractive index at 700nm vs. 865nm (see Appendix C.1.3). Regardless, the fit results of mPLE (0.16 and 0.30) show excellent agreement with mPL.

aligned perpendicular to the substrate. There may also be a tilting of the polymer backbone with respect to the substrate.[60] and we cannot unambiguously identify the cause of differences in TDM orientation between the two morphologies. It is worth noting that the optical technique used here averages both crystalline and amorphous regions and therefore provides different information than can be found from X-ray diffraction alone.

From Lorentz reciprocity[61], momentum-resolved light absorption is formally equivalent to momentum-resolved emission. Using the same principles described above, we provide the first demonstrations of momentum-resolved photoluminescence excitation (mPLE), a proxy for absorption (assuming photoluminescence intensity is linearly proportional to the amount of light absorbed). We collect the total emitted PL (integrated over wavelength and momentum) as a function of the position of our momentum-resolved laser excitation source, Fig. 3.2(b). Face-on and edge-on mPLE measurements are plotted in Figs. 3.5(c) and (d) at an excitation wavelength of 700 nm. Fitting these traces to the appropriate in-plane and out-of-plane basis functions at 700 nm (see Appendix C.1.3), we find out-of-plane to in-plane ratios of 0.16 and 0.30 for face-on and edge-on morphologies respectively. This excellent agreement with momentum-resolved emission (0.13 and 0.29) further validates our observation of larger TDM tilt-angles for edge-on polymer films. This also indicates minimal reorientation of the transition dipole between absorption and emission processes as can occur in other systems [62, 63, 64] which is consistent with the sub-nanosecond lifetimes of excitons in P(NDI2OD-T2).[65, 66, 67, 57]

3.3.3 Spectral differences

The wavelength dependence of these momentum-resolved measurements provides additional insight into the differences in optical properties for the two film morphologies. We only determine mPLE (i.e., absorption) at an excitation wavelength of 700 nm. The

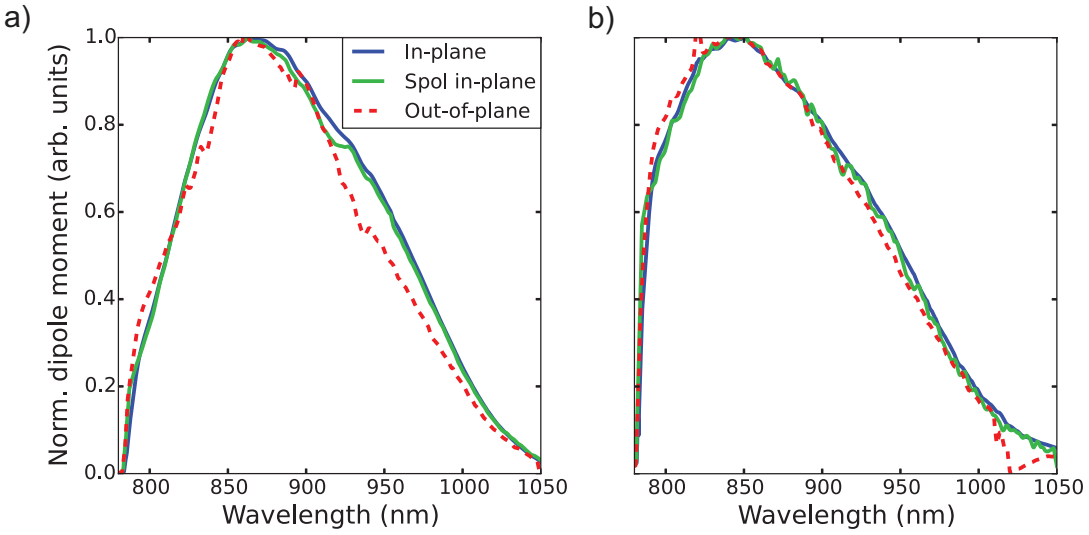

Figure 3.6: In-plane and out-of-plane normalized emission dipole moments for (a) face-on and (b) edge-on P(NDI2OD-T2), determined by performing mPL decompositions across the entire 780-1050 nm emission band.

emitted light, on the other hand, is separated by momentum and wavelength simultaneously. Performing decompositions similar to Fig. 3.4(b), we observe an average OP/IP ratio of 0.12 with a standard deviation of 0.1 across the PL band (750-1050nm) for face-on films. Although the ratio is *mostly* constant across the PL spectrum, deviations from these values are observed primarily at wavelengths to the right of the PL peak. This deviation is most easily visualized by plotting the normalized IP and OP spectra inferred from our fits at each wavelength. For face-on films, Fig. 3.6(a), the s-polarized spectrum (light green), which arises from only IP dipoles, is in close agreement with the IP spectrum determined from fits of p-polarized data (blue, solid). In particular, both spectra reveal a shoulder feature at 950 nm that is absent from the OP spectrum (red, dashed) determined from our fits. In comparison, edge-on films, Fig. 3.6(b) show much closer agreement between all three spectra (the out-of-plane artifact past 1000nm is due to low PL counts throwing off the fitting procedure). Evidently, the spectral dependence of these optical anisotropies reveals subtle differences in the morphology-dependent optical properties that are otherwise obscured.

In previous studies, this 950nm shoulder peak was only seen in aggregated P(NDI2OD-T2).[57]. A likely explanation for the missing face-on shoulder peak is that out-of-plane oriented dipoles are preferentially found in amorphous regions of the sample. When the polymer is initially spin-cast onto the substrate most of the molecules aggregate and align in the plane of the substrate. Some molecules, however, will exist in amorphous regions where there is a more random orientation of the molecules. The low temperature anneal provides only a small amount of energy for the molecules to rearrange and very little of the amorphous regions will crystallize. In this scenario out-of-plane dipoles are preferentially found in these randomly oriented amorphous regions. In contrast, a high temperature anneal, which gives rise to the edge-on morphology, has much more energy for the molecules to adjust and crystallize. A large portion of the amorphous polymers will crystallize while mostly retaining their original orientation. This simple model likely explains why the 950nm shoulder peak corresponding to aggregation is found in the out-of-plane spectra for edge-on, but not face-on, morphologies. To summarize, we expect that the out-of-plane oriented dipole emission in face-on films is coming from amorphous regions. The in-plane dipole emission comes both from amorphous and crystalline regions, but is dominated by the much larger crystalline regions. In edge-on films both out-of-plane and in-plane dipole emission comes from the same crystalline polymers, with a transition dipole moment that is partially oriented perpendicular to the substrate surface.

3.4 Conclusion

In conclusion we use momentum-resolved spectroscopies to measure in-plane and out-of-plane effective dipole moments for face-on and edge-on morphologies of P(NDI2OD-T2). Fits of momentum-resolved emission measurements (mPL) show close agreement

with first-ever analogous absorption measurements using a momentum-resolved photoluminescence excitation (mPLE) technique. We find that edge-on films exhibit a larger out-of-plane tilt angle ($\sim 16^{\circ}$) of the transition dipole moment relative to face-on films ($\sim 7^{\circ}$). These results are consistent with the orientation of the transition dipole moment within NDI planes, but may alternatively be indicative of a difference in average orientation of the polymer backbones. We also observe a missing shoulder peak, characteristic of aggregated P(NDI2OD-T2), in the out-of-plane emission spectrum of face-on films. This suggests that the out-of-plane emission in face-on films arises largely from amorphous regions. As typical optical techniques only measure in-plane oriented dipoles and X-ray diffraction only measures crystalline regions of the film, these out-of-plane amorphous regions have likely been unexplored in previous studies. Finding annealing techniques that maintain face-on orientation while crystallizing these previously hidden regions will likely lead to better charge transport and, therefore, device performance in organic photovoltaics and light-emitting diodes. In addition to these insights on P(NDI2OD-T2)'s morphology, the momentum-resolved techniques developed in this paper can be used to accurately characterize anisotropic optical properties in other materials. These techniques can therefore enable new optimizations of optical device design and reveal subtle differences in morphology that are obscured in other X-ray and optical characterization techniques.

Chapter 4

Preferred orientations in surface plasmon light-trapping architectures

4.1 Abstract

Due to their electric field enhancement, surface plasmon polaritons (SPPs) are capable of drastically increasing light-molecule coupling in organic optoelectronic devices. The electric field enhancement is directional, however, and therefore the concomitant increase in coupling depends on the molecule's orientation with respect to the SPP interface. To investigate this orientation dependence, we studied SPPs in a model system, p-SIDT(FBTTh$_2$)$_2$. We demonstrate that, controllable by processing, p-SIDT(FBTTh$_2$)$_2$ films have either all in-plane or a 50:50 mixture of in-plane and out-of-plane optical dipoles presenting an ideal test bed for orientation-dependent effects. Using momentum-resolved reflectometry and momentum-resolved photoluminescence, we study changes in SPP dispersion and photoluminescence arising purely from molecular orientation. The increased SPP momentum and photoluminescence for out-of-plane oriented molecules agrees well with theory and has direct implications for the design and analysis of organic

optoelectronic devices.

4.2 Introduction

Surface plasmon polaritons (SPPs) are surface electromagnetic waves that may be excited at a metal-dielectric interface [68]. The strong confinement of the SPP modes and consequent large electric field enhancement has attracted a great deal of interest [69]. Indeed, SPPs have wide-ranging applications in organic optoelectronics including light-trapping in organic photovoltaics (OPVs) [70, 71], emission-enhancement in organic light-emitting diodes (OLEDs),[72] and enhanced sensitivity in sensors.[73]

The electric field enhancement from SPPs is highly directional, however. The enhancement in the electric field vector is greatest for the component perpendicular to the interface and small to nonexistent parallel for the component to the interface.[74] While numerous studies on SPP-organic interactions have shown promising results, a systematic experimental demonstration of SPP properties with molecules parallel to the SPP strong electric field direction vs. molecules aligned perpendicular to the field is lacking.

Early work by Drexhage and co-workers studied molecular dyes near metal interfaces. They theoretically calculated that the emission decay rate would depend on molecular orientation.[75] Their experimental demonstrations were limited to molecules parallel to the surface, however.[75] Later experiments with liquid crystals studied changes in molecular tilt angle by measuring SPP position via attenuated total reflection (ATR).[76, 77] Analyzing the results, though, required using a many layer optical model as the molecular orientation of liquid crystal molecules changes with depth under an applied electric field.[78] Other effects on SPPs such as absorption or photoluminescence enhancement were not studied.

Multiple experiments have studied SPPs in uniaxial films with changing in-plane

anisotropy,[79, 80] but only a small handful have investigated the effects on SPPs induced by strong out-of-plane anisotropy.[81, 82] Theoretical studies have looked at changes in the SPP dispersion, propagation length, and absorption in films with significant real and imaginary refractive indices out-of-plane.[83, 9] In particular, organic films with a large out-of-plane imaginary refractive index are expected to have greatly increased efficiency in both plasmonic solar cells and other light-trapping architectures [9]. As molecules aligned out-of-plane are expected to interact most strongly with the SPP electric field, investigating the effects of molecular orientation on SPPs for films with in-plane oriented molecules vs. out-of-plane oriented molecules is of great interest.

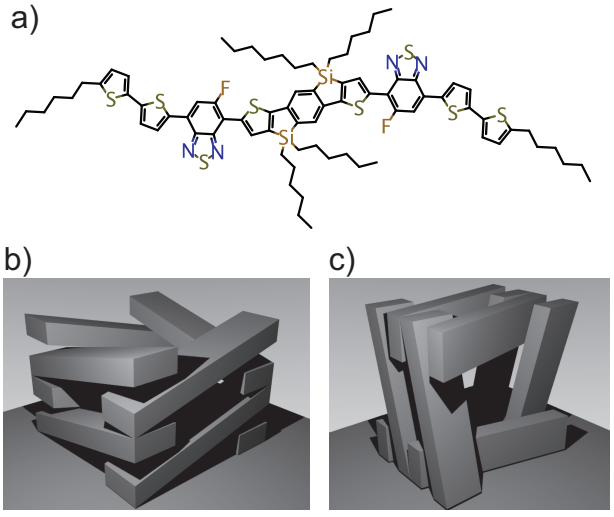

Figure 4.1: (a) The chemical structure of p-SIDT(FBTTh$_2$)$_2$. (b) The structure of the p-SIDT(FBTTh$_2$)$_2$ film cast from dichlorobenzene and (c) the structure of films cast from dichlorobenzene with 0.4% diiodooctane by volume.

In this work we demonstrate the effects of molecular orientation on SPPs by comparing uniaxial organic films with imaginary refractive index either entirely in-plane or evenly split between in-plane and out-of-plane. Crucially, we study films of recently developed p-SIDT(FBTTh$_2$)$_2$ (Figure 4.1a).[84] From grazing incidence wide-angle X-ray scattering (GIWAXS) and transmission electron microscopy (TEM) measurements, it has been shown by Ran and coworkers that p-SIDT(FBTTh$_2$)$_2$ has the unique ability to con-

trollably take on one of two very different orientations.[85] If films are cast directly from chlorobenzene (CB), they take on a face-on orientation with all molecules in the plane of the substrate (Figure 4.1b), while casting from CB with 0.4% by volume diiodooctane (DIO) leads to an edge-on orientation (Figure 4.1c) with a 50:50 mix of in-plane and out-of-plane molecules. This provides the ideal system to study differences in SPPs originating solely from in-plane vs. out-of-plane molecular orientation in a simple geometry with uniform films.

4.3 Results and discussion

To study the SPPs, we use momentum-resolved spectroscopies. These techniques resolve the momentum, or angle, of the light coming from the sample by imaging in the Fourier plane (also known as the back focal plane (BFP)) of the objective. In addition to studying the orientation of emitting and absorbing dipoles in organic films,[18, 14] these spectroscopies have been shown to be excellent for studying SPPs with advantages over typical prism-based approaches.[86]

It is assumed that the optical dipole in p-SIDT(FBTTh$_2$)$_2$ is along the molecular backbone. This is confirmed by momentum-resolved photoluminescence (mPL) spectroscopy of p-SIDT(FBTTh$_2$)$_2$ on quartz (Figure 4.2) which shows that the optical emission dipole strength in face-on films is almost entirely in the plane of the sample while in edge-on films it is a 50:50 mixture of out-of-plane and in-plane orientations. Effective emission dipole strengths were calculated by decomposing emitted light measured via mPL into light coming from in-plane and out-of-plane dipoles using a three layer optical model (see our previous paper[14] for more details). To measure mPL, the sample was excited by a focused 425-650nm light emitting diode (LED) (ThorLabs MCWHL5-C5) that uniformly filled momentum space. The incident light was filtered via a 633nm shortpass filter and

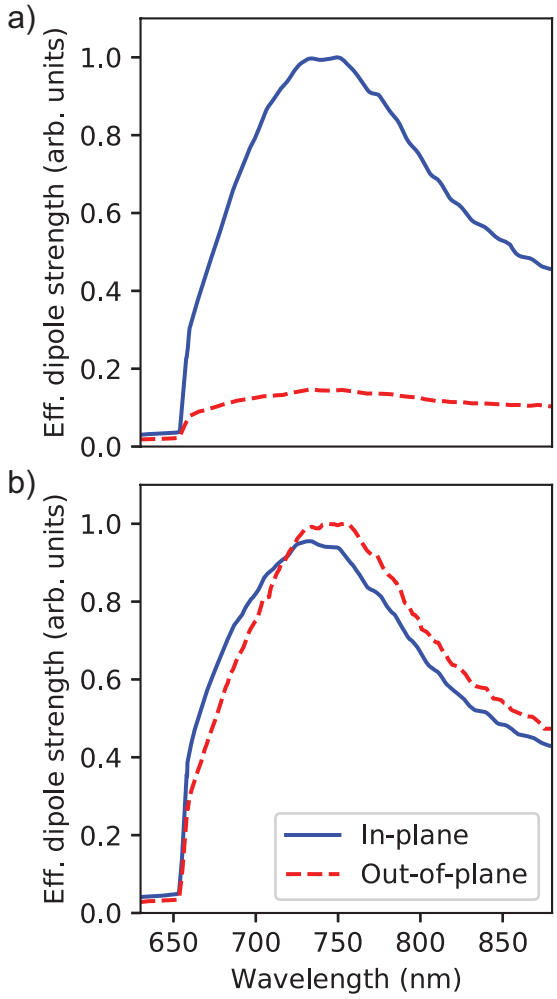

Figure 4.2: Effective emission dipole strengths (a) face-on and (b) edge-on p-SIDT(FBTTh$_2$)$_2$ films on quartz. In-plane (blue, solid line) is parallel to the substrate while out-of-plane (red, dashed line) is perpendicular to the substrate

reflected off a 635nm dichroic mirror to remove overlap with the emission wavelengths. The emitted PL was then filtered to remove excitation reflections by transmitting through the same dichroic as well as a 635nm longpass filter. The PL was then passed through an analyzing polarizer such that light along the y-momentum axis was p-polarized. The energy and y-momentum of the light was then measured by a spectrometer (Princeton Instruments IsoPlane SCT320) with attached charge coupled device (CCD) camera (Princeton Instruments PIXIS 1024BRX) in a BFP conjugate to the objective. The mPL

counts were corrected for momentum-dependent apodization in post-processing.

To map out the energy-momentum dispersion of SPPs for the two molecular orientations, we use mPL spectroscopy and momentum-resolved reflectometry (mR) to measure the momentum of the SPP, k_{SPP}, in thin (20nm) p-SIDT(FBTTh$_2$)$_2$ films on gold as a function of wavelength. The sample structure is shown in Figure 4.3a. Starting with quartz coverslips, a 3nm Ti adhesion layer, and subsequent 44nm Au layer were deposited via thermal evaporation. Films were spin-cast at 3000 RPM from a solution of 10mg/mL p-SIDT(FBTTh$_2$)$_2$ in chlorobenzene (CB). For edge-on films, 0.4% DIO by volume was added to the CB solution. Reflectance was measured in an inverted microscope with a 1.3 numerical aperture (NA) oil immersion objective. A supercontinuum source (SuperK Extreme EXR-15) with a monochromator (NKT Photonics SuperK Select IR2 Vis/NIR) provided the variable wavelength light source. To uniformly illuminate over all incident momenta, a stack of 10 diffuser films was placed in a BFP conjugate to the objective which diffused the incident light to a uniform intensity over the entire BFP. With a CCD camera placed in another conjugate BFP, the reflection intensity at each momentum of light was measured simultaneously (Figure 4.3b). The procedure for measuring mPL (Figure 4.3c) was the same as described above. The reflectance minimum and PL maximum were used to identify the SPP momentum at each wavelength. For a more detailed description of the experimental apparatus, we refer readers to our previous work.[14, 13]

Figure 4.4 shows the SPP dispersion compiled from mR (triangles and circles) and mPL measurements (solid lines) compared to theory (dashed curves) for films of p-SIDT(FBTTh$_2$)$_2$ on Au-Ti-Quartz substrates. The edge-on orientation leads to increased SPP momentum, as well as decreased SPP group velocity ($\frac{\partial \omega}{\partial k}$, indicated by the larger negative slope in the figure), which is consistent with a stronger interaction with the SPP mode. For thicker films this effect will be even more pronounced (see Appendix D, Figure D for the infinitely thick case).

Theory curves were calculated from transfer matrix methods using a four- and five-layer Fresnel model for samples without and with an organic film, respectively. For these curves most system parameters were assumed or determined from reference samples: The refractive index of quartz and the real part of the titanium permittivity were taken from literature.[87, 88] The imaginary part of the Ti permittivity as well as the Au complex permittivity were determined from mR measurements in the absence of organic film (i.e. Figure 4.3, blue circles). The in-plane complex permittivity of p-SIDT$(FBTTh_2)_2$ was measured via mR of p-SIDT$(FBTTh_2)_2$ on quartz. The titanium thickness (3nm) and Au thickness (44nm) were measured via a crystal deposition monitor and refined with mR measurements. Thickness of the p-SIDT$(FBTTh_2)_2$ layer was measured by atomic force microscopy (AFM) to be 20nm. Only the out-of-plane complex permittivity of p-SIDT$(FBTTh_2)_2$ was fit based on the final mR data for substrates with an organic layer.

Figure 4.5 shows the PL intensity for edge-on vs. face-on p-SIDT$(FBTTh_2)_2$ films on Au/Ti/Quartz for each wavelength integrating over all momenta. Due to the emission enhancement of the SPP mode, the maximum edge-on PL was a factor of 2.2 brighter than the equivalent face-on PL. In contrast, edge-on directly on quartz has only 0.9 times the PL as the face-on orientation quartz (Appendix D, Figure D's unnormalized data). This further demonstrates the stronger interaction of the edge-on orientation with the SPP mode.

4.4 Conclusion

In conclusion, we find that edge-on p-SIDT$(FBTTh_2)_2$ films have greater surface plasmon-polariton photoluminescence enhancement and SPP momentum than face-on p-SIDT$(FBTTh_2)_2$ films. We observe a factor of 2.2 greater PL intensity for edge-on vs.

face-on films due to the SPP electric field enhancement. Along with the greater SPP momentum and lower SPP group velocity, this establishes experimentally that edge-on films, and thus out-of-plane oriented molecules, interact more strongly with SPP electric fields. These results highlight the importance of molecular orientation for SPP modes and point to drastically improved organic optoelectronic device performance by aligning molecules to the SPP electric field. Additionally, with measurements of optical dipole orientation in face-on and edge-on films, we introduce p-SIDT(FBTTh$_2$)$_2$ as a model system for studying orientation dependent phenomena in uniaxial media with optical axes out-of-plane. We expect future experiments to study the interplay of optical and electrical performance with molecular orientation to determine the ideal geometry for surface plasmon-polariton devices.

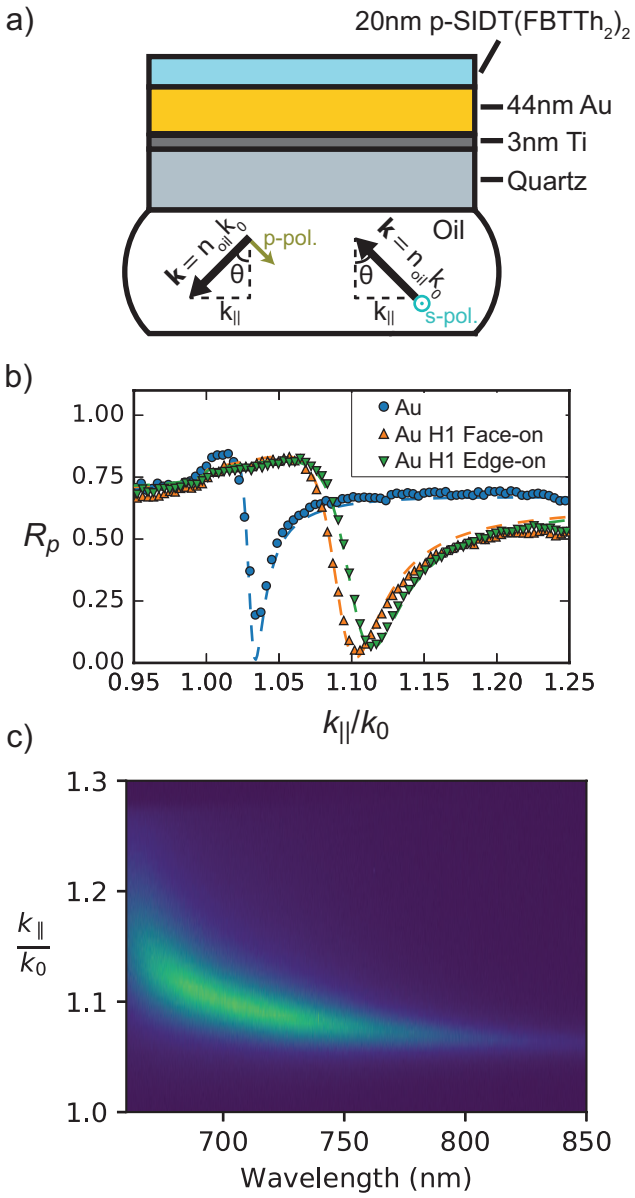

Figure 4.3: (a) Diagram of the sample geometry. (b) Momentum-resolved reflectometry and (c) energy-momentum spectrum of edge-on H1 on Au.

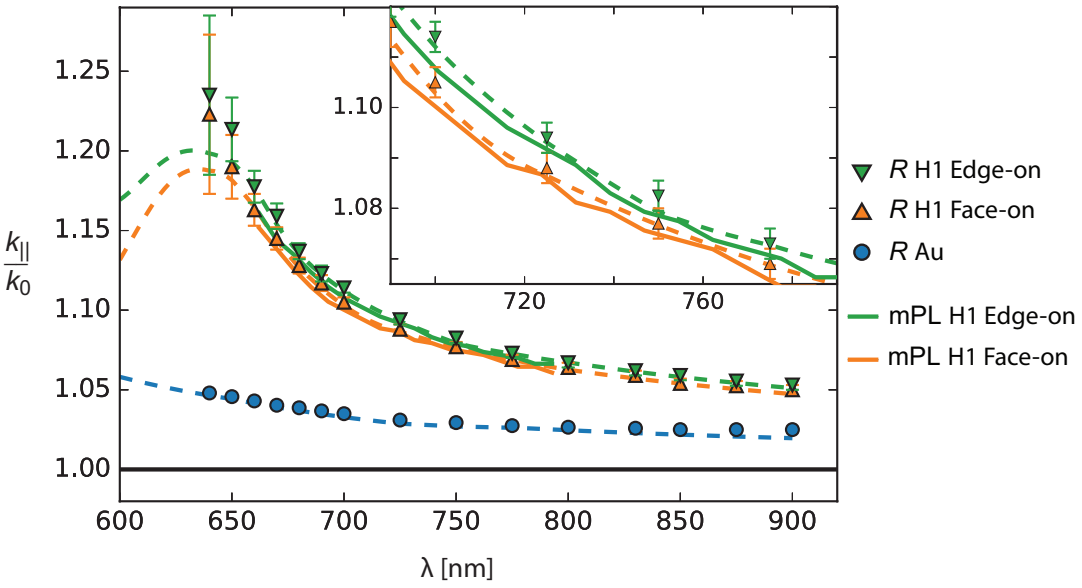

Figure 4.4: The surface plasmon dispersion of edge-on (green) and face-on (orange) films on gold as well as a gold reference (blue) as measured by reflectometry (solid markers) and photoluminescence (solid lines). Theoretical dispersion curves calculated from transfer matrix methods are shown with dashed lines.

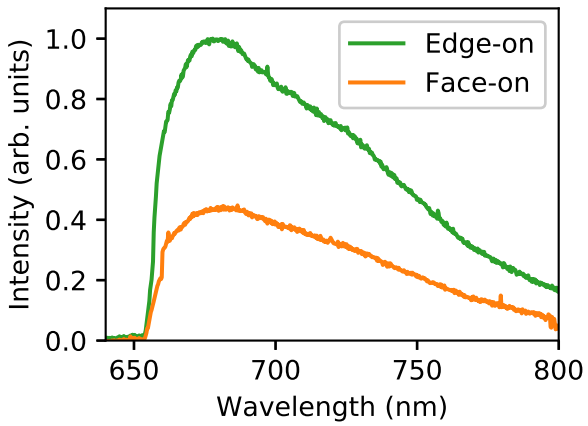

Figure 4.5: The photoluminescence as a function of wavelength for edge-on (green) and face-on (orange) films on gold.

Chapter 5

Outlook and future work

With full resolution of momentum, energy, and polarization for both input and output light, there is tremendous potential for the characterization of optical systems at an unprecedented level of detail. These systems range from molecular emitters to dielectric resonators to excitations in thin films. This chapter will discuss avenues for future research both in organic optoelectronics, which has been the focus of this thesis, and more broadly.

There is a great deal more work to be done investigating optical anisotropies in organic semiconductors. In previous chapters many optical properties were studied by comparisons (e.g. in-plane and out-of-plane dipole strengths). This simplifies the measurements as we only need relative measures as opposed to absolute. It should be possible with precise measurements of the input power and output power of reference and test samples to make absolute measurements. This would enable, for example, determining molecular dipole strengths on an absolute scale. It would then be possible to compare absorption and emission dipole strengths of various molecules (and films) leading to new insights into the relationship between optical properties and molecular structure (and film morphology).

Now that we have the capability to selectively pump purely in-plane or out-of-plane dipoles it should be possible to look at specific excitations in organic semiconductors. For example, Schuller and collaborators were able to identify both intra- and intermolecular excitations in the small molecule 3,4,9,10-perylene tetracarboxylic dianhydride (PTCDA) based on the emitting dipole orientation.[18] With our recent addition of momentum-resolution of incident light, one could pump into intermolecular excitons and observe how the excitations decay into intra- and intermolecular excitons. There is already evidence from the Schuller work that different excitations have different lifetimes.[18] With a pulsed laser and appropriate electronics, time resolution could be added and excitation lifetimes could be measured including if the lifetime changes with the original excited state (previously only the final emitting states could be identified). Another intriguing possibility is investigating if certain excitations have a higher quantum efficiency in organic photovoltaics. We know that molecular orientation plays an important role at the donor-acceptor interface,[89, 85] does excitation orientation play a similar role? By looking at bilayer films as in Ran[85] and adding current-voltage characterization to a momentum-resolved setup, it should be possible to answer these and similar questions.

In this work we have only looked at visible wavelengths and primarily absorption or emission. Using the same techniques, but looking at infrared wavelengths, one could look at vibrational modes in materials. Prior has demonstrated the utility of angle-resolved infrared spectroscopy for studying the orientation of vibrational modes.[45, 60] These spectroscopies could be extended by pumping a specific vibrational mode and watching the decay or seeing how vibrations affect optical excitons as there is significant coupling between the electronic and vibrational modes.[32] In a similar fashion, it should be possible to look at 2D Raman spectra. With full momentum and polarization control on the input and output, the full Raman scattering tensor can be mapped out including the off-diagonal elements usually hidden in goniometer-based measurements. This would

lead to unprecedented detail into the structure and vibrational mechanics of both organic and inorganic films.

Structured light is a huge potential research area. By controlling the light intensity pattern in the back focal plane, by using, for example, a spatial light modulator, specific multipole modes could be excited.[90] This would immediately allow studies of absorption modes in all of the systems mentioned at the beginning of Chapter 2, namely multipole absorption in single molecules, multipole absorption in nanoparticles, magnetic dipole absorption in phosphors, intra- and intermolecular exciton absorption, and absorption into specific nanoantenna modes. There is already some evidence that this fine-grained mode control leads to enhanced device properties.[91] It is also theoretically possible to excite so-called "dark-modes" using structured light.[92] As their name implies, these modes are often hidden to traditional spectroscopy techniques. Note that to achieve the full range of structured light requires 2D patterning of *coherent* light in the back focal plane. This is not possible using other angle-resolved techniques such as goniometers, but is **only possible with full 2D momentum-resolved spectroscopies**. Thus, the apparatus discussed in Chapter 2, with its momentum-resolution of incident light, is uniquely poised to investigate this untapped area of research.

This chapter has touched on some of the areas for future work. Momentum-resolved spectroscopy adds a whole new way of looking at light. While previous work has begun to scratch the surface of what is possible by looking at emitted light, the additional momentum control over incident light introduced in this thesis enables asking a whole new range of research questions both within and outside of organic semiconductors.

Chapter 6

Summary

Organic optoelectronics are inexpensive, made from abundant materials, and tunable. This makes them attractive for many applications including light emitting diodes, photovoltaics, and sensors. While organic light emitting diodes have achieved commercial success, other organic optoelectronic devices, including organic photovoltaics, have not. This is in part due to their low efficiencies making them uncompetitive in the marketplace. Recent work has shown performance in these devices is closely tied to the morphology of the organic semiconductor and many experiments relating the electronic and optical properties of these materials to their structure have been performed. These organic films are highly anisotropic, however, and investigation into the directional-dependence of their optical properties has been lacking. Measuring these optical anisotropies is of interest not only for fundamental science and understanding of organic semiconductor materials but also of practical importance when making devices. In this thesis we have demonstrated momentum-resolved spectroscopies which are particularly well-suited for measuring optical anisotropies, used these spectroscopies to investigate optical and structural anisotropies in organic films, and connected molecular orientation to device performance.

In Chapter 2 we went over how to measure anisotropic optical properties. We covered how to construct and configure a spectroscopy setup to take high precision momentum-resolved photoluminescence, photoluminescence excitation, and reflectometry measurements. We also went through how to analyze the resulting data in detail.

In Chapter 3 we presented results on how optical anisotropies can give insight into the morphology of organic films. We find the tilt angle of the transition dipole moment for two orientations of the polymer P(NDI2OD-T2). We also found regions of disordered polymer in one of the orientations that are challenging to impossible to uncover with traditional X-ray or optical characterization techniques.

In Chapter 4 we demonstrated the effects of molecular orientation in a simple device geometry. We observed surface plasmon polaritons in two very different orientations of the small molecule p-SIDT(FBTTh$_2$)$_2$. Due solely to the molecular orientation there is a shift in the dispersion curve and a factor of 2.4 increase in the photoluminescence of these films. This is consistent with the greater interaction of surface plasmon modes with out-of-plane optical constants and concretely demonstrates the need to take film anisotropy and device geometry into account when finding final performance.

In Chapter 5 many areas of potential future work were identified. Particular attention was paid to applications that take advantage of the incident light momentum-resolution developed in this thesis. The field of structured light was highlighted as the coherent 2D structuring of the light in the back focal plane is only possible using 2D momentum-resolved spectroscopy and cannot be achieved using traditional goniometer techniques which are limited to a single angle of light at a time.

Appendix A

Analysis code

A.1 Edge finding code

```
def find_NA_edges(column, window_size=3, threshold=0.1):
    ''' Finds the edges of transmitted light corresopnding to the NA of the objective '''
    # First smooth the data
    lowess = sm.nonparametric.lowess
    smoothed = lowess(column,range(len(column)), frac= 10/len(column))[:,1]

    # Find edges using a window method
    window_deltas = []
    big_diffs = []

    for (i,e) in enumerate(smoothed):
        window = smoothed[i:i+window_size]
        win_max = max(window)
        win_min = min(window)
        win_diff = win_max - win_min
        window_deltas.append(win_diff)
        if win_diff > threshold*max(smoothed):
            big_diffs.append(i+window.argmin())

    try:
        outside_diffs = [big_diffs[0], big_diffs[-1]]
```

```
    except IndexError:
        outside_diffs=[0,0]

    return outside_diffs
```

A.2 Three layer model code

Python code implementing a three layer model:

```
from __future__ import division
import math
import cmath

class ThreeLayerModel(object):
    """ ThreeLayerModel implments a three layer model to calculate dipole strengths
        for dipoles in the middle layer
    """
    def __init__(self, n1o, n1e, n2o, n2e, n3, dist_to_layer_3, dist_to_layer_1):
        ''' n1o                 Ordinary refractive index in top layer
            n1e                 Extraordinary refractive index in top layer
            n2o                 Ordinary refractive index in emitter (middle) layer
            n2e                 Extraordinary refractive index in emitter (middle) layer
            n3                  Refractive index in substrate (input and collection) layer
            dist_to_layer_3     Distance from emitter to layer 3
            dist_to_layer_1     Distance from emitter to layer 1
        '''

        # Input parameters
        self.n1o = n1o
        self.n1e = n1e
        self.n2o = n2o
        self.n2e = n2e
        self.n3 = n3
        self.dist_to_layer_3 = dist_to_layer_3
        self.dist_to_layer_1 = dist_to_layer_1

        # Calculated parameters
        self.layer_2_thickness = self.dist_to_layer_1 + self.dist_to_layer_3 # nm
```

```
def calc_dipole_emission(self, ky_normed, wavelength, eff_dipole_strengths, apo_factor=True):
    ''' Calculates the expected emission at ky_normed momentum on the detector for both
        polarizations given an electric diople with [in-plane, out-of-plane] effective dipole
        strengths.

        ky_normed             ky in units of k_0 (also Sin(theta)*n3 for angle theta) in layer 3
        wavelength            Wavelength in nm
        eff_dipole_strengths  [in-plane, out-of-plane] effective dipole strengths of the emitter
        apo_factor            Whether to include an apodization factor of 1/Cos(theta)
    '''

    # Calculated parameters
    speed_of_light = 3*10**17 # nanometers/sec
    k_0 = 2*math.pi/wavelength # 1/nm

    # Wavevectors
    ky = k_0 * ky_normed # 1/nm
    kz1s = cmath.sqrt((self.n1o*k_0)**2-ky**2) # s-polarized in layer 1
    kz2s = cmath.sqrt((self.n2o*k_0)**2-ky**2) # s-polarized in layer 2
    kz3s = cmath.sqrt((self.n3*k_0)**2-ky**2) # s-polarized in layer 3
    kz1p = cmath.sqrt((self.n1o*k_0)**2-(ky*self.n1o/self.n1e)**2) # p-pol in layer 1
    kz2p = cmath.sqrt((self.n2o*k_0)**2-(ky*self.n2o/self.n2e)**2) # p-pol in layer 2
    kz3p = cmath.sqrt((self.n3*k_0)**2-ky**2) # p-pol in layer 3 (currently same as kz3s since
                                              # layer 3 assumed isotropic)

    # Coefficients
    # transmission coefficient from layer 3 into layer 2 for s- and p-polarizations
    ts32 = 2*kz3s/(kz3s+kz2s)
    tp32 = (2*self.n2o**2*kz3p/(self.n2o**2*kz3p+self.n3**2*kz2p)*
          self.n3/(self.n2o))

    # reflection coefficient from layer 2 to 1 for s- and p-polarizations
    rs21 = (kz2s-kz1s)/(kz2s+kz1s)
    rp21 = (self.n1o**2*kz2p-self.n2o**2*kz1p)/(self.n1o**2*kz2p+self.n2o**2*kz1p)

    # reflection coefficient from layer 2 to 3 for s- and p-polarizations
    rs23 = (kz2s-kz3s)/(kz2s+kz3s)
    rp23 = (self.n3**2*kz2p-self.n2o**2*kz3p)/(self.n3**2*kz2p+self.n2o**2*kz3p)
```

```
# Grouped parameters
if apo_factor == True:
    grouped_As = (speed_of_light/wavelength**2)*(1/(4*k_0**2))*(k_0/kz3s)
    grouped_Ap = (speed_of_light/wavelength**2)*(1/(4*k_0**2))*(k_0/kz3p)
elif apo_factor == False:
    grouped_As = (speed_of_light/wavelength**2)*(1/(4*k_0**2))*1/self.n3
    grouped_Ap = (speed_of_light/wavelength**2)*(1/(4*k_0**2))*1/self.n3
grouped_Bs = 1 - rs21*rs23*cmath.exp(2*1j*kz2s*self.layer_2_thickness)
grouped_Bp = 1 - rp21*rp23*cmath.exp(2*1j*kz2p*self.layer_2_thickness)
# [DISCLAIMER]
# hbar and the vacuum perimittivity should appear in C_0's denominator, but they are
# set to one here as we're in arbitrary units anyways
grouped_C0 = (2*math.pi)**3/(wavelength**3*math.pi)

# Normalized LDOS for electric dipoles
#
# norm_rho_sx => norm_rho_s_IP
# norm_rho_py => norm_rho_p_IP
# norm_rho_pz => norm_rho_p_OP
norm_rho_sx = abs(grouped_As *
              abs(
                (
                (ts32*cmath.exp(1j*kz2s*self.dist_to_layer_1))*
                (1+rs21*cmath.exp(2j*kz2s*self.dist_to_layer_3))
                )
              /grouped_Bs)**2
              )
norm_rho_py = abs(grouped_Ap *
              abs(
                (
                (tp32*cmath.exp(1j*kz2p*self.dist_to_layer_1)*kz2p/(self.n2o*k_0))*
                (1-rp21*cmath.exp(2j*kz2p*self.dist_to_layer_3))
                )
              /grouped_Bp)**2
              )
norm_rho_pz = abs(grouped_Ap *
              abs(
                (
```

```
                    (tp32*cmath.exp(1j*kz2p*self.dist_to_layer_1)*ky/(self.n2o*k_0))*
                    (self.n2o/self.n2e)**2*
                    (1+rp21*cmath.exp(2j*kz2p*self.dist_to_layer_3))
                    )
                   /grouped_Bp)**2
                   )

        # Calculate emission counts (in arbitrary units since there are unknown experimental
        # constants) -- I multiply by 10^-9 to normalize near 1 which makes fitting easier
        counts_ppol = grouped_C0 * (norm_rho_py*eff_dipole_strengths[0] +
                                    norm_rho_pz*eff_dipole_strengths[1]) * 10**-9
        counts_spol = grouped_C0 * (norm_rho_sx*eff_dipole_strengths[0]) * 10**-9

        return (counts_ppol, counts_spol)
```

A.3 Dipole strength code

```
freom __future__ import division
from scipy import optimize
import numpy as np
import pandas as pd
import statsmodels.api as sm
import scipy.integrate as integrate
import math
import cmath

class MplDipoleStrengths(object):
    """ MplDipoleStrength finds the in-plane and out-of-plane effective emission dipole strengths
    """

    def __init__(self, model, data):
        ''' model           Three layer model of the sample
            data            Data frame containing 'wavelength', 'row', 'column', and 'counts'
                            columns. The counts should be for light emitted with p-polarization.
                            Fitting works best if counts are normalized near 1.
        '''
        self.model = model
        self.data = data
```

```
        self.wavelengths = {}
        self.count_array = None


    def reshape_counts(self):
        ''' Reshape counts into a 2d numpy array. Also creates a dictionary with columns as keys
            and wavelengths as values.
        '''
        # Set up column -> wavelength dictionary
        for i, wavelength in enumerate(self.data['wavelength'].unique()):
            self.wavelengths[i] = wavelength

        # Reshape counts into appropriate rectangular array
        num_rows = len(self.data['row'].unique())
        num_cols = len(self.data['column'].unique())
        self.count_array = self.data['counts'].reshape((num_rows,num_cols))


    def assign_ky(self, column):
        ''' Takes a column of counts and assigns ky values to them
        '''
        # First find the column PL edges which we correspond to ky = 1.3 k_0
        edges = self.find_NA_edges(column)

        # We expect edges[0] < edges[1]
        if edges[0] >= edges[1]:
            return None

        num_rows = len(column)
        ky_list = np.zeros(num_rows)
        mid = int((edges[0] + edges[1])/2) # The mid point between k_0's is ky = 0
        ky_per_pix = 2.6/(edges[1] - edges[0])

        for i in range(num_rows):
            ky_list[i] = (mid-i)*ky_per_pix
        return ky_list

    def find_NA_edges(self, column, window_size=3, threshold=0.1):
        ''' Finds the edges of transmitted light corresopnding to the NA of the objective '''
```

```
        # First smooth the data
        lowess = sm.nonparametric.lowess
        smoothed = lowess(column,range(len(column)), frac= 10/len(column))[:,1]

        # Find edges using a window method
        window_deltas = []
        big_diffs = []

        for (i,e) in enumerate(smoothed):
            window = smoothed[i:i+window_size]
            win_max = max(window)
            win_min = min(window)
            win_diff = win_max - win_min
            window_deltas.append(win_diff)
            if win_diff > threshold*max(smoothed):
                big_diffs.append(i+window.argmin())

        try:
            outside_diffs = [big_diffs[0], big_diffs[-1]]
        except IndexError:
            outside_diffs=[0,0]

        return outside_diffs


    def cost_func(self, dip_strengths, column, ky_list, wavelength):
        ''' Returns the summed square error for actual vs. predicted counts across ky's

            Inputs
            --------
            wavelength is in nanometers.
            dip_strengths is a list of effective dipole strengths with 2 real-valued elements.
                [in-plane_dip_strength, out-plane_dip_strength]
        '''
        num_rows = len(column)
        square_errors = np.zeros(num_rows)
        theo_ppol = np.zeros(num_rows)

        for i,ky in enumerate(ky_list):
```

```
            theo_ppol[i] = self.model.calc_dipole_emission(ky_normed=ky, wavelength=wavelength,
                                                           eff_dipole_strengths=dip_strengths)[0]
        square_errors = (column - theo_ppol)**2
        return square_errors.sum()


    def fit_dip_strengths_col(self, column, wavelength, init_strengths=[1,1]):
        ''' Returns the fit effective dipole strengths along with scipy.optimize's summary output.

            Returns a tuple with (in-plane_eff_dip_strength, out-plane_eff_dip_strength).
            With perfect data (no noise) the error (cost-function) is convex with respect to the
            fitting parameters so fitting should be fast and converge to the correct value.

            Inputs
            --------
            wavelength is in nanometers.
            init_strengths sets the initial strengths to start the minimization algorithm.
        '''
        ky_list = self.assign_ky(column)

        # Error handling: if for some reason assign_ky doesn't return at least 2 unique values
        if type(ky_list) == type(None) or len(np.unique(ky_list)) < 2:
            return (0,0)

        # Figure out the entries with |ky| < 1.15
        # Since ky_list is reverse sorted I take negate the values so search sorted works properly
        first_index = (-ky_list).searchsorted(-1.15, side='right')
        last_index = (-ky_list).searchsorted(1.15, side='left')
        return optimize.fmin_bfgs(self.cost_func,init_strengths,
                                  args=(column[first_index:last_index],
                                        ky_list[first_index:last_index],
                                        wavelength),
                                  full_output = False,
                                  disp = False
                                 )


    def fit_dip_strengths(self, init_strengths=[1,1]):
        ''' Returns a dataframe with 'wavlength', 'in-plane strength', and 'out-plane strength'
```

```
            columns.
        '''
        # Check if we've reshaped the data yet
        if type(self.count_array) == type(None):
            self.reshape_counts()

        wavelength_col = []
        in_plane_strengths = []
        out_plane_strengths = []
        for i,col in enumerate(self.count_array.T):
            # Keep track of progress
            if i % 100 == 0:
                print("On column {0}".format(i))
            wavelength = self.wavelengths[i]
            wavelength_col.append(wavelength)
            strengths = self.fit_dip_strengths_col(col, wavelength, init_strengths)
            in_plane_strengths.append(strengths[0])
            out_plane_strengths.append(strengths[1])
        return pd.DataFrame({'wavelength':wavelength_col, 'in-plane':in_plane_strengths,
                             'out-plane':out_plane_strengths})

    def ip_counts(self, dip_strengths, ky, wavelength):
        ''' Returns (ppol, spol) counts from in-plane dipoles at a given ky and wavelength by setting
            out-of-plane dipole strength to 0.
        '''
        return self.model.calc_dipole_emission(ky_normed=ky, wavelength=wavelength,
                                               eff_dipole_strengths=[dip_strengths[0], 0])

    def op_counts(self, dip_strengths, ky, wavelength):
        ''' Returns (ppol, spol) counts from out-of-plane dipoles at a given ky and wavelength by setting
            in-plane dipole strength to 0.
        '''
        return self.model.calc_dipole_emission(ky_normed=ky, wavelength=wavelength,
                                               eff_dipole_strengths=[0, dip_strengths[1]])

    def calc_ppol_count_ratio(self, dip_strengths, wavelength, ky_max=1.15):
        ''' Returns the integrated ppol count ratio up to ky_max '''
        op_int = integrate.quad(lambda x:self.op_counts(dip_strengths, x, wavelength)[0],
                                -ky_max, ky_max)
```

```
        ip_int = integrate.quad(lambda x:self.ip_counts(dip_strengths, x, wavelength)[0],
                                -ky_max, ky_max)
        return op_int[0]/ip_int[0]

    def calc_in_plane_dipole_from_spol(self, spol_df, ky_normed=0):
        ''' Calculates the in-plane dipole strength given spol counts at ky_normed.

            :param spol_df: Pandas dataframe. Contains 'counts' and 'wavelength' columns.
                There should only be one counts entry per wavelength.
            :param ky_normed: Float. ky in units of k_0 in layer 3.
            :return: Pandas dataframe. Contains 'in-plane' and 'wavelength' columns.
        '''
        SPEED_OF_LIGHT = 3*10**17 # nanometers/sec
        in_plane_strengths = []

        for wavelength in spol_df['wavelength']:
            k_0 = 2*math.pi/wavelength # 1/nm

            # Wavevectors
            ky = k_0 * ky_normed # 1/nm
            kz1s = cmath.sqrt((self.model.n1o*k_0)**2-ky**2) # s-polarized in layer 1
            kz2s = cmath.sqrt((self.model.n2o*k_0)**2-ky**2) # s-polarized in layer 2
            kz3s = cmath.sqrt((self.model.n3*k_0)**2-ky**2) # s-polarized in layer 3
            kz1p = cmath.sqrt((self.model.n1o*k_0)**2-
                              (ky*self.model.n1o/self.model.n1e)**2) # p-pol in layer 1
            kz2p = cmath.sqrt((self.model.n2o*k_0)**2-
                              (ky*self.model.n2o/self.model.n2e)**2) # p-pol in layer 2
            kz3p = cmath.sqrt((self.model.n3*k_0)**2-ky**2) # p-pol in layer 3 (currently same as
                                                            # kz3s since layer 3 assumed isotropic)

            # Coefficients
            # transmission coefficient from layer 3 into layer 2 for s- and p-polarizations
            ts32 = 2*kz3s/(kz3s+kz2s)
            tp32 = (2*self.model.n2o**2*kz3p/(self.model.n2o**2*kz3p+self.model.n3**2*kz2p)*
                    self.model.n3/(self.model.n2o))

            # reflection coefficient from layer 2 to 1 for s- and p-polarizations
            rs21 = (kz2s-kz1s)/(kz2s+kz1s)
            rp21 = ((self.model.n1o**2*kz2p-self.model.n2o**2*kz1p)/
```

```
                (self.model.n1o**2*kz2p+self.model.n2o**2*kz1p))

        # reflection coefficient from layer 2 to 3 for s- and p-polarizations
        rs23 = (kz2s-kz3s)/(kz2s+kz3s)
        rp23 = (self.model.n3**2*kz2p-self.model.n2o**2*kz3p)/(self.model.n3**2*kz2p+self.model.n2o**2*kz3p)



        grouped_Bs = 1 - rs21*rs23*cmath.exp(2*1j*kz2s*self.model.layer_2_thickness)
        grouped_As = (SPEED_OF_LIGHT/wavelength**2)*(1/(4*k_0**2))*(k_0/kz3s)
        norm_rho_sx = abs(grouped_As *
                          abs(
                              (
                                  (ts32*cmath.exp(1j*kz2s*self.model.dist_to_layer_1))*
                                  (1+rs21*cmath.exp(2j*kz2s*self.model.dist_to_layer_3))
                              )
                              /grouped_Bs)**2
                         )
        grouped_C0 = (2*math.pi)**3/(wavelength**3*math.pi)
        counts = spol_df.loc[spol_df.wavelength == wavelength,'counts'].values[0]
        strength = counts/(grouped_C0*norm_rho_sx*10**-9)
        in_plane_strengths.append([wavelength, strength])
    return pd.DataFrame(in_plane_strengths, columns=['wavelength','in-plane'])


def get_linecuts(self):
    ''' Returns a dataframe with the values of the pixels at -k_0, 0, and +k_0 at each
        wavelength.
    '''
    wavelength = []
    minus_k_0 = []
    zero_k_0 = []
    plus_k_0 = []

    # Check if we've reshaped the data yet
    if type(self.count_array) == type(None):
         self.reshape_counts()

    # Find the above values column by column
    for i,col in enumerate(self.count_array.T):
        wavelength.append(self.wavelengths[i])
```

```
        ky_list = self.assign_ky(col)
        if type(ky_list) == type(None):
            minus_k_0.append(0)
            zero_k_0.append(0)
            plus_k_0.append(0)

        else:
            # Figure out the entries with |ky| = 1
            # Since ky_list is reverse sorted I take negate the values so search sorted works properly
            minus_index = (-ky_list).searchsorted(1, side='left')
            zero_index = (-ky_list).searchsorted(0, side='right')
            plus_index = (-ky_list).searchsorted(-1, side='right')

            minus_k_0.append(col[minus_index])
            zero_k_0.append(col[zero_index])
            plus_k_0.append(col[plus_index])

    return pd.DataFrame({'-k_0': minus_k_0, '0': zero_k_0, '+k_0': plus_k_0},
                        index = wavelength)
```

Appendix B

Optical alignment procedure

1. Focus a sample (one that fluoresces if possible to decouple the input and output focusing) by eye in real space in the microscope. Use the 0.5 - 1.3 NA variable numerical aperture oil immersion objective.

2. Focus and align output optics

   (a) Make sure that you can see photoluminescence on the spectrometer camera. If you cannot see PL, check that the microscope is set to send light out the left (L) side, an appropriate filter set is in use, light is actually being output on the emission side, the spectrometer slit is **not** in place, and the grating is set to 0nm to capture the zeroth order reflection. If you still cannot see PL, adjust periscope mirrors and, if necessary, gently move spectrometer so that the light appears on the camera.

   (b) Focus the output lens so the back focal plane is in focus

      i. Illuminate the sample at normal incidence or uniformly in the back focal plane. If the sample is illuminated non-uniformly in the back focal plane at a high momentum, there could be correlation between input angle and

the output intensity's angular distribution due to apodization effects in the objective.

ii. Set variable NA objective to 0.5 NA.

iii. Focus output lens until edge of photoluminescence is visibly sharp. It may help to look at the intensity slope at the edge of PL for fine focusing – a sharper slope is more in focus. You may only be able to focus one side of the PL image at a time at this stage. Try to focus roughly in the middle of the nearest and farthest focus.

(c) Align output optics

i. First make sure output lens is square/flat with respect to the microscope output.

ii. Center the output lens with respect to the microscope output so that the light travels through the center of the lens.

iii. Make sure center height of each periscope mirror is the same height as the microscope light output and spectrometer light input for the first and second periscope mirror respectively.

iv. Adjust the mirror tilts by turning the tilt knobs on the mirror mounts. Think of the light as having a flat constant-phase front; this phase front should go into the spectrometer flush so that each point in the back focal plane travels the same distance and is simultaneously in focus. To get close to flush, use the big knob on top of the top mirror mount to sweep the light beam around the room. Adjust the tilt knobs on both mirror mounts until the light beam sweeps flat around the room at the height of the of the spectrometer input. Use the big knob on the top of the mirror mount to send the light into the spectrometer once more. Looking at the

2D back focal plane image, make fine adjustments to the mirror tilts until the top and bottom (most important) as well as left and right of the image (less important) are symmetric in intensity. It may help to refocus the output lens during this final step.

v. Refocus the output lens. The top and bottom as well as left and right of the back focal plane image should now be in focus at the same position of the output lens.

3. Align and focus input optics for laser fiber input (if using laser fiber input)

(a) Switch filters and/or sample so that the reflected light can be imaged on the camera.

(b) If the input path has been removed, start by adjusting the optics so they are square/flush with respect to the microscope input entrance. This can be done by temporarily placing machined parts with two flat side between the microscope input and optic mount and then rotating the optic mount until it is flat. Next, center the input lens by using the 50:50 mirror on the filter wheel, turning on the overhead lamp, and looking at the reflected light sent "backwards" on the input side of the input lens using a piece of paper or lens paper. When the lens is properly centered, the light will focus uniformly as you move the paper straight back from the lens. If it is not centered, the focus will move off-center with respect to the lens.

(c) Align the laser fiber by first adjusting the mount until it is square/flush with the input lens mount (and therefore the microscope). Center the laser fiber by moving its reflection spot on the camera using the motorized translation stage until it is at the center of the back focal plane.

(d) Focus the laser fiber. It is easier to focus if the laser fiber is slightly off-center in the back focal plane, thereby avoiding the reflections near normal incidence. Move the laser fiber closer or farther from the input lens using the motorized stage until the laser spot is focused on the camera. It should have roughly 3-5 pixels full-width half-max using the variable 0.5-1.3 NA objective at visible wavelengths. Fine focusing is achieved by maximizing the center intensity of the laser spot as measured on the camera.

4. Align and focus the LED mirror (if using LED input)

(a) First make sure the LED mount is flat with respect to the table using supporting mounts. It has a tendency to sag if not supported.

(b) With the LED off, move the mirror such that the center of the mirror is vertically and horizontally centered with respect to the microscope input entrance. Adjust the mirror such that is forms a 45 degree angle with respect to the LED.

(c) With the LED on, adjust the mirror rotation and position until the reflect light is visible on the camera. Adjust slowly; if moving too fast you may not see the reflected light and overshoot.

(d) Focus the mirror by moving it closer or farther away from the LED. The reflected light should completely fill the back focal plane up to the NA of the objective and be as bright as possible.

(e) "Flatten" light in back focal plane by adjusting mirror rotation, height, and tilt. When properly aligned the top and bottom as well as left and right of the back focal plane image should be the same intensity. It has sometimes been necessary in this step to place pieces of paper under the mirror mounting post

to tilt the mirror with respect to the table.

Appendix C

Chapter 3 additional details

This appendix contains additional details for Chapter 4.

C.1 Methods

C.1.1 Experimental setup

By placing a detector in the back focal plane of a microscope objective, Fig. C.1, we separate light based on the angle, or momentum, at which it leaves the sample. A spectrometer (Princeton Instruments IsoPlane SCT320) coupled to a 2D CCD camera (Princeton Instruments PIXIS 1024BRX) separates light by wavelength along one axis of the camera and momentum along the other axis. This allows measurements of momentum-dependent photoluminescence intensity at many wavelengths simultaneously. From this data, we separate emission spectra from dipoles oriented in-plane and out-of-plane. For mPL experiments we used a collimated LED source (ThorLabs M735L3-C5) to excite the sample across all momenta uniformly.

Similarly to how placing a detector in a conjugate back focal plane to the objective allowed us to study emission of different momenta of light, we placed our excitation source

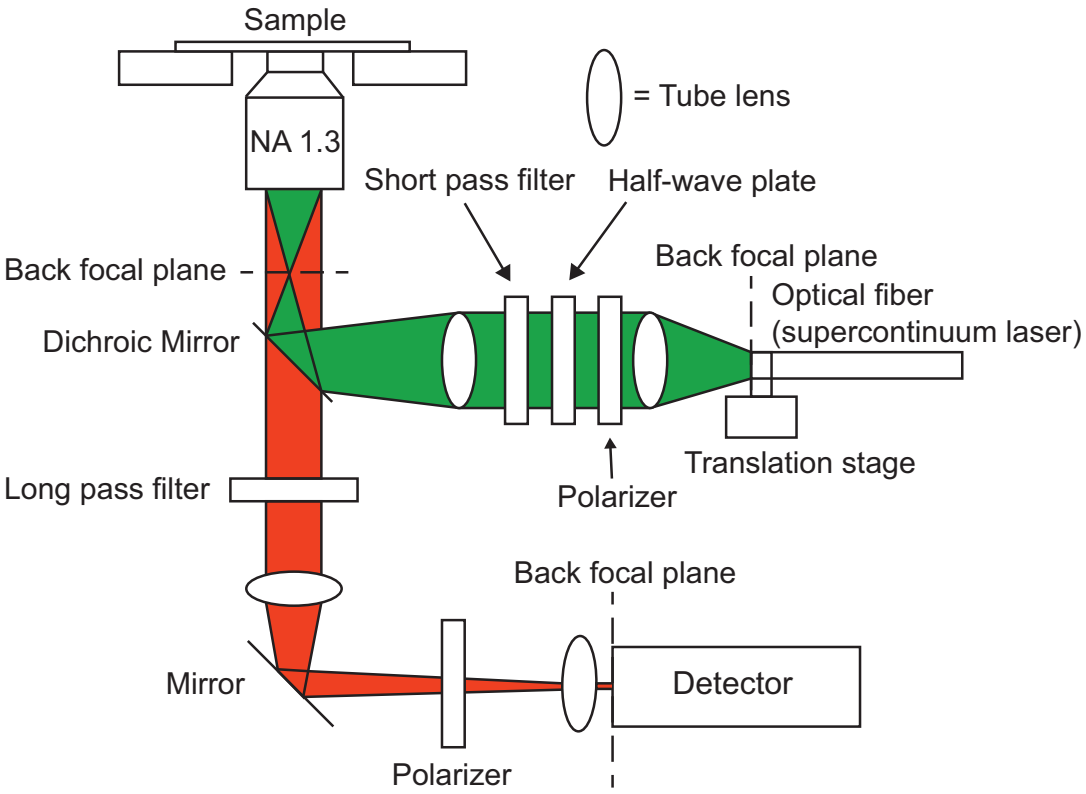

Figure C.1: The momentum-resolved setup used in the experiments. For momentum-resolved photoluminescence, the supercontinuum excitation source along with the half-wave plate, polarizer, and first tube lens were replaced with a collimated LED.

in another conjugate back focal plane to study absorption as a function of light momenta. We studied absorption properties by measuring the integrated intensity of photoluminescence emitted from the sample versus the input excitation momentum (similar to how photoluminescence excitation, or PLE, measures PL versus input wavelength of light). The end of a single mode optical fiber (coming from a fiber-coupled supercontinuum source (SuperK Extreme EXR-15)) was mounted on a translation stage. By moving the end of the fiber within the conjugate back focal plane, we control the incident momentum vector of the light exciting the sample.

C.1.2 Sample fabrication

P(NDI2OD-T2) (Polyera ActivInk N2200) was spin-cast from 1,2-dichlorobenzene solution (10 µg/mL). Samples were then annealed at 150 °C for one hour to produce face-on samples or at 305 °C for one hour to produce edge-on samples. The samples were then allowed to slowly cool to room temperature. Film thickness was measured using atomic force microscopy (AFM) to be 50nm. Glass, 200nm silicon dioxide on silicon, and quartz coverslip substrates were used for AFM, ellipsometry, and PL measurements respectively.

C.1.3 Data analysis

Raw camera images were analyzed using Python. In mPL we obtain a rectangular image with wavelength varying along the x-axis and momentum varying along the y-axis. To obtain in-plane and out-of-plane emission dipole moments, we analyzed each wavelength independently. For a given wavelength column in the p-polarized image, we first converted the pixels of the camera into units of k_0 by setting the edges of PL to the 1.3 NA ($\pm 1.3k_0$) of our microscope objective. After converting to units of momentum, we used a three layer model (following the treatment in Schuller *et al.*[18]) to solve for the linear combination of in-plane and out-of-plane effective emission dipole moments that summed to the intensity vs. momentum shape measured at each wavelength. The model's input parameters—refractive index and film thickness—were determined from ellipsometry and AFM measurements respectively. After fitting p-polarized data, we determine the expected s-polarized PL intensity vs. momentum and compare to actual s-polarized measurements.

Data analysis for mPLE was similar, but had many separate images that needed to be aggregated. For each PL image the exciting laser y-position was determined by taking the

image of the reflected laser spot without the PL filter. Each PL image was background subtracted using a "window frame" of dark pixels that surrounded the pixels receiving PL in the center of the image. This allowed us to correct for background drift over time. The background subtracted PL image was then summed across all pixels to determine a single PL value for each image. From the PL image, we were able to convert pixels to k_0 as above. We then found the linear combination of in-plane and out-of-plane effective absorption dipole moments that summed to the counts vs. momentum shape observed. Again, we determine the expected s-polarized PL intensity vs. incident momentum and compare to actual s-polarized measurements. It is important to note that while the mPL model includes an apodization factor, given the setup geometry the mPLE model does not. In mPL, each pixel of fixed width in the back-focal-plane correspond to a different magnitude of solid-angle over which the PL is collected. Thus, an isotropic emitter would still exhibit intensity variations across the back focal plane image. In mPLE, the solid-angle magnitude also changes, but the input power is fixed and no correction is needed.

Dipole moments found via mPL and mPLE are highly sensitive to the film refractive indices input in the three-layer model (especially in the out-of-plane direction). For this reason it is essential to have accurate optical constants. We used atomic force microscopy, UV-Vis transmission, and ellipsometry to get accurate thickness, in-plane extinction coefficient, and refractive indices respectively.

C.2 Supplemental Material

Figure C.S1 shows grazing incidence wide-angle X-ray scattering (GIWAXS) for the two orientations of P(NDI2OD-T2). The (100) peak at roughly 0.25 $\mathring{A}^{-1}$ indicates the orientation of the alkyl chain stacking direction along with the higher order (200), (300),

and (400) peaks at 0.5 $\mathring{A}^{-1}$, 0.75 $\mathring{A}^{-1}$, and 1.0 $\mathring{A}^{-1}$, respectively.

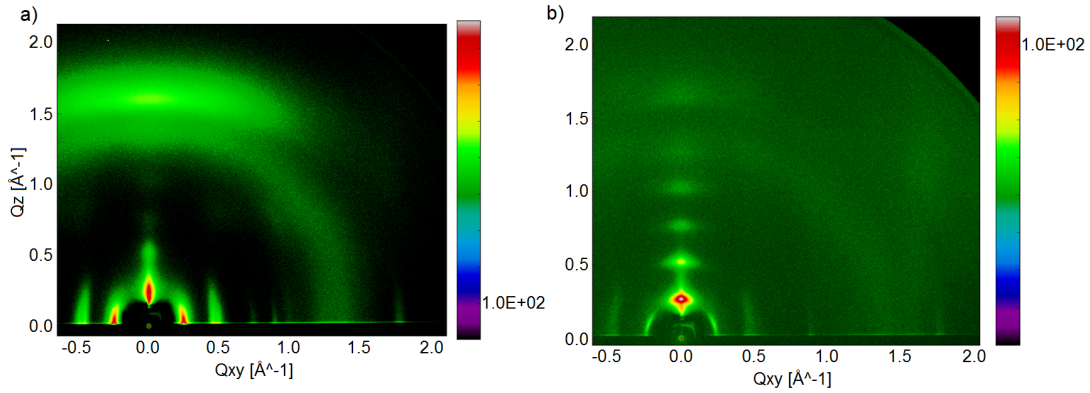

Figure C.S1: a)Grazing incidence wide-angle X-ray scattering (GIWAXS) for a face-on oriented P(NDI2OD-T2) annealed at 150°C for 6 hours and b)for an edge-on oriented P(NDI2OD-T2) annealed at 300°C for 45 minutes.

For reference, variable angle spectroscopic ellipsometry (VASE) measurements on P(NDI2OD-T2) are provided in Figure C.S2. Note the ellipsometry seems to indicate that the face-on orientation has more out-of-plane oriented dipoles, which is not what we would expect from the measurements or theory in Chapter 3.

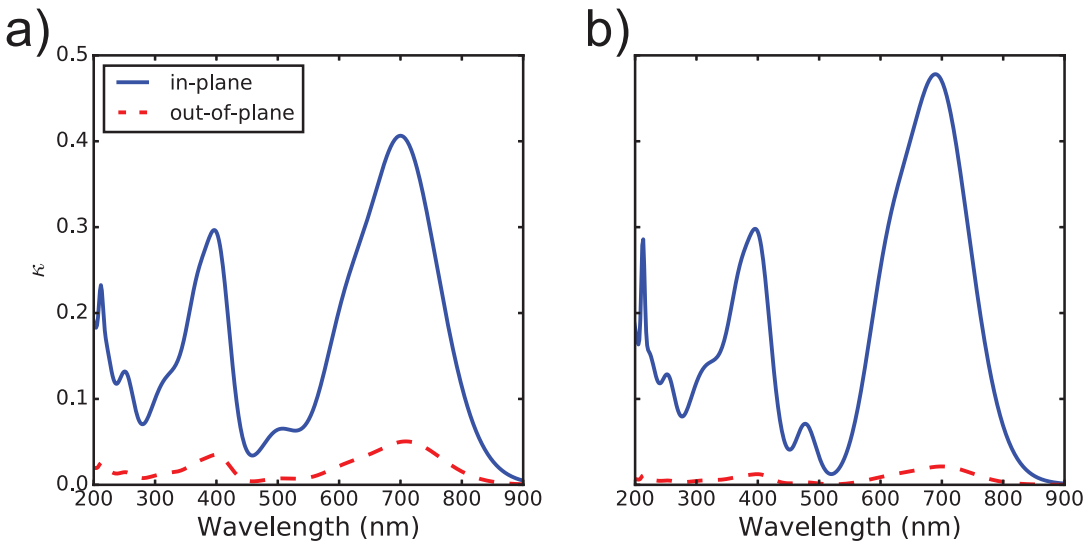

Figure C.S2: The extinction coefficient in the in-plane and out-of-plane directions (with respect to the substrate) for (a) face-on and (b) edge-on P(NDI2OD-T2), determined from spectroscopic ellipsometry measurements. The ellipsometry results are highly model dependent and unable to capture the differences in optical anisotropies that are evident in momentum-resolved measurements.

Appendix D

Chapter 4 additional details

This appendix contains additional details for Chapter 4.

Figure D.S1 is a calculation of the dispersion of infinitely thick p-SIDT(FBTTh$_2$)$_2$ films on Au. Note not only the increased momentum and difference between edge-on (green, dot-dash) and face-on (orange, dashed) curves, but also the increased negative slope of the edge-on curve indicative of reduced surface plasmon polariton group velocity.

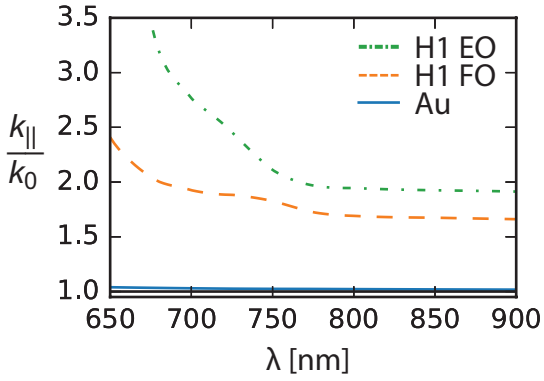

Figure D.S1: Calculated dispersion curves for infinitely thick edge-on (green, dot-dash) and face-on (orange, dashed) p-SIDT(FBTTh$_2$)$_2$ films on Au.

Figure D.S2 displays y-polarized photoluminescence 2D back focal plane images for a) face-on and b) edge-on p-SIDT(FBTTh$_2$)$_2$ films. The in-plane character of the face-on

film and the mixed character of the edge-on film provide additional support for the dipole strengths shown in figure 4.2.

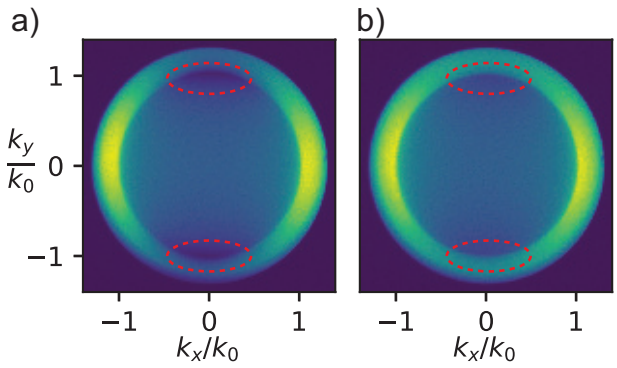

Figure D.S2: Back focal plane images of y-polarized photoluminescence from a) face-on and b) edge-on p-SIDT(FBTTh$_2$)$_2$ films on quartz. The face-on image has the pattern of an in-plane dipole while the edge-on image has the pattern of an out-of-plane dipole. The red dotted ovals highlight the critical angle where this difference is most pronounced. The intensity has been normalized to highlight the differences in pattern.

Bibliography

[1] S. R. Forrest, *The path to ubiquitous and low-cost organic electronic appliances on plastic*, *Nature* **428** (Apr., 2004) 911–918.

[2] Y. Shirota, *Organic materials for electronic and optoelectronic devicesBasis of a presentation given at Materials Chemistry Discussion No. 2, 1315 September 1999, University of Nottingham, UK.*, *Journal of Materials Chemistry* **10** (2000), no. 1 1–25.

[3] S. R. Forrest and M. E. Thompson, *Introduction: Organic Electronics and Optoelectronics*, *Chemical Reviews* **107** (Apr., 2007) 923–925.

[4] M. A. Green, K. Emery, Y. Hishikawa, W. Warta, and E. D. Dunlop, *Solar cell efficiency tables (version 42)*, *Progress in Photovoltaics: Research and Applications* **21** (2013), no. 5 827–837.

[5] B. P. Rand, D. Cheyns, K. Vasseur, N. C. Giebink, S. Mothy, Y. Yi, V. Coropceanu, D. Beljonne, J. Cornil, J.-L. Brdas, and J. Genoe, *The Impact of Molecular Orientation on the Photovoltaic Properties of a Phthalocyanine/Fullerene Heterojunction*, *Advanced Functional Materials* **22** (2012), no. 14 2987–2995.

[6] H. Sirringhaus, P. J. Brown, R. H. Friend, M. M. Nielsen, K. Bechgaard, B. M. W. Langeveld-Voss, A. J. H. Spiering, R. a. J. Janssen, E. W. Meijer, P. Herwig, and D. M. d. Leeuw, *Two-dimensional charge transport in self-organized, high-mobility conjugated polymers*, *Nature* **401** (Oct., 1999) 685–688.

[7] P. M. Beaujuge and J. M. J. Frchet, *Molecular Design and Ordering Effects in -Functional Materials for Transistor and Solar Cell Applications*, *Journal of the American Chemical Society* **133** (Dec., 2011) 20009–20029.

[8] M. Shah, V. Pryamitsyn, and V. Ganesan, *Effect of anisotropic charge transport on device characteristics of polymer solar cells*, *Applied Physics Letters* **95** (Nov., 2009) 194101.

[9] R. R. Grote, S. J. Brown, J. B. Driscoll, R. M. Osgood, and J. A. Schuller, *Morphology-dependent light trapping in thin-film organic solar cells*, *Optics Express* **21** (Sept., 2013) A847–A863.

[10] V. C. Sundar, J. Zaumseil, V. Podzorov, E. Menard, R. L. Willett, T. Someya, M. E. Gershenson, and J. A. Rogers, *Elastomeric Transistor Stamps: Reversible Probing of Charge Transport in Organic Crystals*, *Science* **303** (Mar., 2004) 1644–1646.

[11] C. Reese and Z. Bao, *High-Resolution Measurement of the Anisotropy of Charge Transport in Single Crystals*, *Advanced Materials* **19** (Dec., 2007) 4535–4538.

[12] M. Campoy-Quiles, J. Nelson, P. G. Etchegoin, D. D. C. Bradley, V. Zhokhavets, G. Gobsch, H. Vaughan, A. Monkman, O. Ingnas, N. K. Persson, H. Arwin, M. Garriga, M. I. Alonso, G. Herrmann, M. Becker, W. Scholdei, M. Jahja, and C. Bubeck, *On the determination of anisotropy in polymer thin films: A comparative study of optical techniques*, *physica status solidi (c)* **5** (2008), no. 5 1270–1273.

[13] R. A. DeCrescent, S. J. Brown, R. A. Schlitz, M. L. Chabinyc, and J. A. Schuller, *Model-blind characterization of thin-film optical constants with momentum-resolved reflectometry*, *Optics Express* **24** (Dec., 2016) 28842–28857.

[14] S. J. Brown, R. A. Schlitz, M. L. Chabinyc, and J. A. Schuller, *Morphology-dependent optical anisotropies in the n-type polymer P(NDI2od-T2)*, *Physical Review B* **94** (Oct., 2016) 165105.

[15] M. A. Lieb, J. M. Zavislan, and L. Novotny, *Single-molecule orientations determined by direct emission pattern imaging*, *Journal of the Optical Society of America B* **21** (June, 2004) 1210–1215.

[16] P. Woniak, P. Banzer, and G. Leuchs, *Selective switching of individual multipole resonances in single dielectric nanoparticles*, *Laser & Photonics Reviews* **9** (Mar., 2015) 231–240.

[17] T. H. Taminiau, S. Karaveli, N. F. van Hulst, and R. Zia, *Quantifying the magnetic nature of light emission*, *Nature Communications* **3** (July, 2012) 979.

[18] J. A. Schuller, S. Karaveli, T. Schiros, K. He, S. Yang, I. Kymissis, J. Shan, and R. Zia, *Orientation of luminescent excitons in layered nanomaterials*, *Nature Nanotechnology* **8** (Apr., 2013) 271–276.

[19] K. Hassan, A. Bouhelier, T. Bernardin, G. Colas-des Francs, J.-C. Weeber, A. Dereux, and R. Espiau de Lamaestre, *Momentum-space spectroscopy for advanced analysis of dielectric-loaded surface plasmon polariton coupled and bent waveguides*, *Physical Review B* **87** (May, 2013) 195428.

[20] A. G. Curto, G. Volpe, T. H. Taminiau, M. P. Kreuzer, R. Quidant, and N. F. v. Hulst, *Unidirectional Emission of a Quantum Dot Coupled to a Nanoantenna*, *Science* **329** (Aug., 2010) 930–933.

[21] J. A. Kurvits, M. Jiang, and R. Zia, *Comparative analysis of imaging configurations and objectives for Fourier microscopy*, *JOSA A* **32** (Nov., 2015) 2082–2092.

[22] K. A. Mazzio and C. K. Luscombe, *The future of organic photovoltaics*, *Chemical Society Reviews* **44** (Dec., 2014) 78–90.

[23] L. S. Hung and C. H. Chen, *Recent progress of molecular organic electroluminescent materials and devices*, *Materials Science and Engineering: R: Reports* **39** (Dec., 2002) 143–222.

[24] D. M. DeLongchamp, R. J. Kline, D. A. Fischer, L. J. Richter, and M. F. Toney, *Molecular Characterization of Organic Electronic Films*, *Advanced Materials* **23** (2011), no. 3 319–337.

[25] D. M. DeLongchamp, R. J. Kline, E. K. Lin, D. A. Fischer, L. J. Richter, L. A. Lucas, M. Heeney, I. McCulloch, and J. E. Northrup, *High Carrier Mobility Polythiophene Thin Films: Structure Determination by Experiment and Theory*, *Adv. Mater.* **19** (Mar., 2007) 833–837.

[26] N. D. Treat, J. A. Nekuda Malik, O. Reid, L. Yu, C. G. Shuttle, G. Rumbles, C. J. Hawker, M. L. Chabinyc, P. Smith, and N. Stingelin, *Microstructure formation in molecular and polymer semiconductors assisted by nucleation agents*, *Nature Materials* **12** (July, 2013) 628–633.

[27] Y. Diao, B. C.-K. Tee, G. Giri, J. Xu, D. H. Kim, H. A. Becerril, R. M. Stoltenberg, T. H. Lee, G. Xue, S. C. B. Mannsfeld, and Z. Bao, *Solution coating of large-area organic semiconductor thin films with aligned single-crystalline domains*, *Nature Materials* **12** (July, 2013) 665–671.

[28] B.-G. Kim, E. J. Jeong, J. W. Chung, S. Seo, B. Koo, and J. Kim, *A molecular design principle of lyotropic liquid-crystalline conjugated polymers with directed alignment capability for plastic electronics*, *Nature Materials* **12** (July, 2013) 659–664.

[29] R. Noriega, J. Rivnay, K. Vandewal, F. P. V. Koch, N. Stingelin, P. Smith, M. F. Toney, and A. Salleo, *A general relationship between disorder, aggregation and charge transport in conjugated polymers*, *Nat Mater* **12** (Aug., 2013) 10388–1044.

[30] D. Venkateshvaran, M. Nikolka, A. Sadhanala, V. Lemaur, M. Zelazny, M. Kepa, M. Hurhangee, A. J. Kronemeijer, V. Pecunia, I. Nasrallah, I. Romanov, K. Broch, I. McCulloch, D. Emin, Y. Olivier, J. Cornil, D. Beljonne, and H. Sirringhaus,

Approaching disorder-free transport in high-mobility conjugated polymers, *Nature* **515** (Nov., 2014) 384–388.

[31] J. Cabanillas-Gonzalez, G. Grancini, and G. Lanzani, *Pump-Probe Spectroscopy in Organic Semiconductors: Monitoring Fundamental Processes of Relevance in Optoelectronics*, *Advanced Materials* **23** (2011), no. 46 5468–5485.

[32] F. C. Spano, *The Spectral Signatures of Frenkel Polarons in H- and J-Aggregates*, *Accounts of Chemical Research* **43** (Mar., 2010) 429–439.

[33] B. J. Schwartz, *Conjugated Polymers as Molecular Materials: How Chain Conformation and Film Morphology Influence Energy Transfer and Interchain Interactions*, *Annual Review of Physical Chemistry* **54** (2003), no. 1 141–172.

[34] M. Campoy-Quiles, P. G. Etchegoin, and D. D. C. Bradley, *On the optical anisotropy of conjugated polymer thin films*, *Physical Review B* **72** (July, 2005) 045209.

[35] K. Tremel, F. S. U. Fischer, N. Kayunkid, R. D. Pietro, R. Tkachov, A. Kiriy, D. Neher, S. Ludwigs, and M. Brinkmann, *Charge Transport Anisotropy in Highly Oriented Thin Films of the Acceptor Polymer P(NDI2od-T2)*, *Adv. Energy Mater.* **4** (July, 2014) 1301659.

[36] C. Soci, D. Comoretto, F. Marabelli, and D. Moses, *Anisotropic photoluminescence properties of oriented poly(p-phenylene-vinylene) films: Effects of dispersion of optical constants*, *Phys. Rev. B* **75** (Feb., 2007) 075204.

[37] D. T. James, B. K. C. Kjellander, W. T. T. Smaal, G. H. Gelinck, C. Combe, I. McCulloch, R. Wilson, J. H. Burroughes, D. D. C. Bradley, and J.-S. Kim, *Thin-Film Morphology of Inkjet-Printed Single-Droplet Organic Transistors Using Polarized Raman Spectroscopy: Effect of Blending TIPS-Pentacene with Insulating Polymer*, *ACS Nano* **5** (Dec., 2011) 9824–9835.

[38] S. Kotarba, J. Jung, A. Kowalska, T. Marszalek, M. Kozanecki, P. Miskiewicz, M. Mas-Torrent, C. Rovira, J. Veciana, J. Puigmarti-Luis, and J. Ulanski, *Anisotropy in structural and physical properties in tetrathiafulvalene derivatives-based zone-cast layers as seen by Raman spectroscopy, UV-visible spectroscopy, and field effect measurements*, *Journal of Applied Physics* **108** (July, 2010) 014504.

[39] T. D. Schmidt, D. S. Setz, M. Flmmich, J. Frischeisen, D. Michaelis, C. Mayr, A. F. Rausch, T. Wehlus, B. J. Scholz, T. C. G. Reusch, N. Danz, and W. Brtting, *Comprehensive efficiency analysis of organic light-emitting diodes featuring emitter orientation and triplet-to-singlet up-conversion*, *Applied Physics Letters* **103** (Aug., 2013) 093303.

[40] M. Grell and D. D. C. Bradley, *Polarized Luminescence from Oriented Molecular Materials*, *Advanced Materials* **11** (Aug., 1999) 895–905.

[41] S. B. Jo, H. H. Kim, H. Lee, B. Kang, S. Lee, M. Sim, M. Kim, W. H. Lee, and K. Cho, *Boosting Photon Harvesting in Organic Solar Cells with Highly Oriented Molecular Crystals via Graphene-Organic Heterointerface*, *ACS Nano* **9** (July, 2015) 8206–8219.

[42] T. Ellenbogen and K. B. Crozier, *Exciton-polariton emission from organic semiconductor optical waveguides*, *Physical Review B* **84** (Oct., 2011) 161304.

[43] C. J. Takacs, N. D. Treat, S. Krmer, Z. Chen, A. Facchetti, M. L. Chabinyc, and A. J. Heeger, *Remarkable Order of a High-Performance Polymer*, *Nano Letters* **13** (June, 2013) 2522–2527.

[44] E. Gann, C. R. McNeill, M. Szumilo, H. Sirringhaus, M. Sommer, S. Maniam, S. J. Langford, and L. Thomsen, *Near-edge X-ray absorption fine-structure spectroscopy of naphthalene diimide-thiophene co-polymers*, *The Journal of Chemical Physics* **140** (Apr., 2014) 164710.

[45] E. Giussani, D. Fazzi, L. Brambilla, M. Caironi, and C. Castiglioni, *Molecular Level Investigation of the Film Structure of a High Electron Mobility Copolymer via Vibrational Spectroscopy*, *Macromolecules* **46** (Apr., 2013) 2658–2670.

[46] N. Martino, D. Fazzi, C. Sciascia, A. Luzio, M. R. Antognazza, and M. Caironi, *Mapping Orientational Order of Charge-Probed Domains in a Semiconducting Polymer*, *ACS Nano* **8** (June, 2014) 5968–5978.

[47] T. Schuettfort, L. Thomsen, and C. R. McNeill, *Observation of a Distinct Surface Molecular Orientation in Films of a High Mobility Conjugated Polymer*, *Journal of the American Chemical Society* **135** (Jan., 2013) 1092–1101.

[48] M. Brinkmann, E. Gonthier, S. Bogen, K. Tremel, S. Ludwigs, M. Hufnagel, and M. Sommer, *Segregated versus Mixed Interchain Stacking in Highly Oriented Films of Naphthalene Diimide Bithiophene Copolymers*, *ACS Nano* **6** (Nov., 2012) 10319–10326.

[49] A. M. Anton, R. Steyrleuthner, W. Kossack, D. Neher, and F. Kremer, *Spatial Orientation and Order of Structure-Defining Subunits in Thin Films of a High Mobility n-Type Copolymer*, *Macromolecules* **49** (Mar., 2016) 1798–1806.

[50] D. Fazzi and M. Caironi, *Multi-length-scale relationships between polymer molecular structure and charge transport: the case of poly-naphthalene diimide bithiohene*, *Physical Chemistry Chemical Physics* **17** (Feb., 2015) 8573–85900.

[51] M. Caironi, M. Bird, D. Fazzi, Z. Chen, R. Di Pietro, C. Newman, A. Facchetti, and H. Sirringhaus, *Very Low Degree of Energetic Disorder as the Origin of High Mobility in an n-channel Polymer Semiconductor*, *Advanced Functional Materials* **21** (Sept., 2011) 3371–3381.

[52] S. Fabiano, H. Yoshida, Z. Chen, A. Facchetti, and M. A. Loi, *Orientation-Dependent Electronic Structures and Charge Transport Mechanisms in Ultrathin Polymeric n-Channel Field-Effect Transistors*, *ACS Applied Materials & Interfaces* **5** (May, 2013) 4417–4422.

[53] V. D'Innocenzo, A. Luzio, A. Petrozza, D. Fazzi, and M. Caironi, *Nature of Charge Carriers in a High Electron Mobility Naphthalenediimide Based Semiconducting Copolymer*, *Advanced Functional Materials* **24** (Sept., 2014) 5584–5593.

[54] A. Luzio, L. Criante, V. D'Innocenzo, and M. Caironi, *Control of charge transport in a semiconducting copolymer by solvent-induced long-range order*, *Sci. Rep.* **3** (Dec., 2013) 3425.

[55] J. Rivnay, R. Steyrleuthner, L. H. Jimison, A. Casadei, Z. Chen, M. F. Toney, A. Facchetti, D. Neher, and A. Salleo, *Drastic Control of Texture in a High Performance n-Type Polymeric Semiconductor and Implications for Charge Transport*, *Macromolecules* **44** (July, 2011) 5246–5255.

[56] T. Schuettfort, S. Huettner, S. Lilliu, J. E. Macdonald, L. Thomsen, and C. R. McNeill, *Surface and Bulk Structural Characterization of a High-Mobility Electron-Transporting Polymer*, *Macromolecules* **44** (Mar., 2011) 1530–1539.

[57] R. Steyrleuthner, M. Schubert, I. Howard, B. Klaumnzer, K. Schilling, Z. Chen, P. Saalfrank, F. Laquai, A. Facchetti, and D. Neher, *Aggregation in a High-Mobility n-Type Low-Bandgap Copolymer with Implications on Semicrystalline Morphology*, *J. Am. Chem. Soc.* **134** (Nov., 2012) 18303–18317.

[58] E. Pavlopoulou, C. S. Kim, S. S. Lee, Z. Chen, A. Facchetti, M. F. Toney, and Y.-L. Loo, *Tuning the Morphology of All-Polymer OPVs through Altering PolymerSolvent Interactions*, *Chemistry of Materials* **26** (Sept., 2014) 5020–5027.

[59] N.-K. Kim, S.-Y. Jang, G. Pace, M. Caironi, W.-T. Park, D. Khim, J. Kim, D.-Y. Kim, and Y.-Y. Noh, *High-Performance Organic Field-Effect Transistors with Directionally Aligned Conjugated Polymer Film Deposited from Pre-Aggregated Solution*, *Chemistry of Materials* **27** (Dec., 2015) 8345–8353.

[60] E. Giussani, L. Brambilla, D. Fazzi, M. Sommer, N. Kayunkid, M. Brinkmann, and C. Castiglioni, *Structural Characterization of Highly Oriented Naphthalene-Diimide-Bithiophene Copolymer Films via Vibrational Spectroscopy*, *The Journal of Physical Chemistry B* **119** (Feb., 2015) 2062–2073.

[61] R. J. Potton, *Reciprocity in optics*, *Reports on Progress in Physics* **67** (2004), no. 5 717.

[62] A. Montali, C. Bastiaansen, P. Smith, and C. Weder, *Polarizing energy transfer in photoluminescent materials for display applications*, *Nature* **392** (Mar., 1998) 261–264.

[63] M. Forster, D. Thomsson, P. R. Hania, and I. G. Scheblykin, *Redistribution of emitting state population in conjugated polymers probed by single-molecule fluorescence polarization spectroscopy*, *Physical Chemistry Chemical Physics* **9** (Feb., 2007) 761–766.

[64] B. J. Schwartz, T.-Q. Nguyen, J. Wu, and S. H. Tolbert, *Interchain and intrachain exciton transport in conjugated polymers: ultrafast studies of energy migration in aligned MEH-PPV/mesoporous silica composites*, *Synthetic Metals* **116** (Jan., 2001) 35–40.

[65] K. Szendrei, D. Jarzab, Z. Chen, A. Facchetti, and M. A. Loi, *Ambipolar all-polymer bulk heterojunction field-effect transistors*, *J. Mater. Chem.* **20** (Feb., 2010) 1317–1321.

[66] Z. Li, J. D. A. Lin, H. Phan, A. Sharenko, C. M. Proctor, P. Zalar, Z. Chen, A. Facchetti, and T.-Q. Nguyen, *Competitive Absorption and Inefficient Exciton Harvesting: Lessons Learned from Bulk Heterojunction Organic Photovoltaics Utilizing the Polymer Acceptor P(NDI2od-T2)*, *Advanced Functional Materials* **24** (Nov., 2014) 6989–6998.

[67] J. R. Moore, S. Albert-Seifried, A. Rao, S. Massip, B. Watts, D. J. Morgan, R. H. Friend, C. R. McNeill, and H. Sirringhaus, *Polymer Blend Solar Cells Based on a High-Mobility Naphthalenediimide-Based Polymer Acceptor: Device Physics, Photophysics and Morphology*, *Advanced Energy Materials* **1** (2011), no. 2 230–240.

[68] J. M. Pitarke, V. M. Silkin, E. V. Chulkov, and P. M. Echenique, *Theory of surface plasmons and surface-plasmon polaritons*, *Reports on Progress in Physics* **70** (2007), no. 1 1.

[69] J. Zhang, L. Zhang, and W. Xu, *Surface plasmon polaritons: physics and applications*, *Journal of Physics D: Applied Physics* **45** (2012), no. 11 113001.

[70] D. M. Callahan, J. N. Munday, and H. A. Atwater, *Solar Cell Light Trapping beyond the Ray Optic Limit*, *Nano Letters* **12** (Jan., 2012) 214–218.

[71] Q. Gan, F. J. Bartoli, and Z. H. Kafafi, *Plasmonic-Enhanced Organic Photovoltaics: Breaking the 10% Efficiency Barrier*, *Advanced Materials* **25** (May, 2013) 2385–2396.

[72] A. Fujiki, T. Uemura, N. Zettsu, M. Akai-Kasaya, A. Saito, and Y. Kuwahara, *Enhanced fluorescence by surface plasmon coupling of Au nanoparticles in an organic electroluminescence diode*, *Applied Physics Letters* **96** (Jan., 2010) 043307.

[73] A. G. Brolo, R. Gordon, B. Leathem, and K. L. Kavanagh, *Surface Plasmon Sensor Based on the Enhanced Light Transmission through Arrays of Nanoholes in Gold Films*, *Langmuir* **20** (June, 2004) 4813–4815.

[74] L. Novotny and B. Hecht, *Surface plasmons*, in *Principles of Nano-Optics*, pp. 378–416. Cambridge University Press, first ed., 2006.

[75] K. H. Drexhage, *IV Interaction of Light with Monomolecular Dye Layers*, in *Progress in Optics* (E. Wolf, ed.), vol. 12, pp. 163–232. Elsevier, 1974. DOI: 10.1016/S0079-6638(08)70266-X.

[76] K. R. Welford and J. R. Sambles, *Detection of surface director reorientation in a nematic liquid crystal*, *Applied Physics Letters* **50** (Apr., 1987) 871–873.

[77] K. R. Welford, J. R. Sambles, and M. G. Clark, *Guided modes and surface plasmon-polaritons observed with a nematic liquid crystal using attenuated total reflection*, *Liquid Crystals* **2** (Jan., 1987) 91–105.

[78] G. J. Sprokel, R. Santo, and J. D. Swalen, *Determination of the Surface Tilt Angle by Attenuated Total Reflection*, *Molecular Crystals and Liquid Crystals* **68** (June, 1981) 29–38.

[79] Y. Takeichi, Y. Kimoto, M. Fujii, and S. Hayashi, *Anisotropic propagation of surface plasmon polaritons induced by para-sexiphenyl nanowire films*, *Physical Review B* **84** (Aug., 2011) 085417.

[80] R. Li, C. Cheng, F.-F. Ren, J. Chen, Y.-X. Fan, J. Ding, and H.-T. Wang, *Hybridized surface plasmon polaritons at an interface between a metal and a uniaxial crystal*, *Applied Physics Letters* **92** (Apr., 2008) 141115.

[81] X. Wang, P. Wang, J. Chen, Y. Lu, H. Ming, and Q. Zhan, *Theoretical and experimental studies of surface plasmons excited at metal-uniaxial dielectric interface*, *Applied Physics Letters* **98** (Jan., 2011) 021113.

[82] H. Wang, *Anisotropic effects of columnar structure on attenuated total reflection experiments*, *Optics Communications* **135** (Feb., 1997) 257–263.

[83] A. A. Krokhin, A. Neogi, and D. McNeil, *Long-range propagation of surface plasmons in a thin metallic film deposited on an anisotropic photonic crystal*, *Physical Review B* **75** (June, 2007) 235420.

[84] J. A. Love, I. Nagao, Y. Huang, M. Kuik, V. Gupta, C. J. Takacs, J. E. Coughlin, L. Qi, T. S. van der Poll, E. J. Kramer, A. J. Heeger, T.-Q. Nguyen, and G. C. Bazan, *Silaindacenodithiophene-Based Molecular Donor: Morphological Features and Use in the Fabrication of Compositionally Tolerant, High-Efficiency Bulk Heterojunction Solar Cells*, *Journal of the American Chemical Society* **136** (Mar., 2014) 3597–3606.

[85] N. A. Ran, S. Roland, J. A. Love, V. Savikhin, C. J. Takacs, Y.-T. Fu, H. Li, V. Coropceanu, X. Liu, J.-L. Brdas, G. C. Bazan, M. F. Toney, D. Neher, and T.-Q. Nguyen, *Impact of Interfacial Molecular Orientation on Radiative Recombination and Charge Generation Efficiencies*, *Submitted*.

[86] D. G. Zhang, X. Yuan, and A. Bouhelier, *Direct image of surface-plasmon-coupled emission by leakage radiation microscopy*, *Applied Optics* **49** (Feb., 2010) 875–879.

[87] I. H. Malitson, *Interspecimen Comparison of the Refractive Index of Fused Silica*,*, *JOSA* **55** (Oct., 1965) 1205–1209.

[88] P. B. Johnson and R. W. Christy, *Optical Constants of the Noble Metals*, *Physical Review B* **6** (Dec., 1972) 4370–4379.

[89] J. R. Tumbleston, B. A. Collins, L. Yang, A. C. Stuart, E. Gann, W. Ma, W. You, and H. Ade, *The influence of molecular orientation on organic bulk heterojunction solar cells*, *Nature Photonics* **8** (May, 2014) 385–391.

[90] T. Das, P. P. Iyer, R. A. DeCrescent, and J. A. Schuller, *Beam engineering for selective and enhanced coupling to multipolar resonances*, *Physical Review B* **92** (Dec., 2015) 241110.

[91] G. Pirruccio, M. Ramezani, S. R.-K. Rodriguez, and J. G. Rivas, *Coherent Control of the Optical Absorption in a Plasmonic Lattice Coupled to a Luminescent Layer*, *Physical Review Letters* **116** (Mar., 2016) 103002.

[92] T. Das and J. A. Schuller, *Dark modes and field enhancements in dielectric dimers illuminated by cylindrical vector beams*, *Physical Review B* **95** (May, 2017) 201111.